Chapter 4
Data Science-Based Battery Operation Management I

This chapter focuses on the data science technologies for battery operation management, which is another key and intermediate process in the full-lifespan of battery. After manufacturing, battery would be operated in various applications such as transportation electrification, stationary energy storage and smart grid to supply or absorb the power, where suitable management solutions are necessary to ensure its efficiency, safety, and sustainability. In this context, numerous state-of-the-art data science strategies have been developed to perform efficient management of battery operation.

To systematically illustrate the data science-based strategies for benefitting battery operation management, an overview is first given to introduce several crucial parts of battery operation management, which includes battery operation modelling, battery state estimation, battery lifetime prognostics, battery fault diagnosis, and battery charging. Then the fundamentals of battery operation modelling as well as state estimation are detailed in this chapter, while the latter three operation parts will be described in the next chapter. Besides, case studies of deriving proper data science methods to benefit four crucial state estimations of battery are all presented and analysed.

4.1 Battery Operation Modelling

Establishing a suitable battery model is generally the starting point for battery operation management [1]. Over the years, numerous data science-based battery operation models with different levels of accuracy and complexity have been designed. This section mainly focuses on three typical types of battery operation models including battery electrical model, battery thermal model, and battery coupled model, which are widely adopted to capture battery operational dynamics, as detailed in Fig. 4.1.

K. Liu et al., *Data Science-Based Full-Lifespan Management of Lithium-Ion Battery*, Green Energy and Technology,
https://doi.org/10.1007/978-3-031-01340-9_4

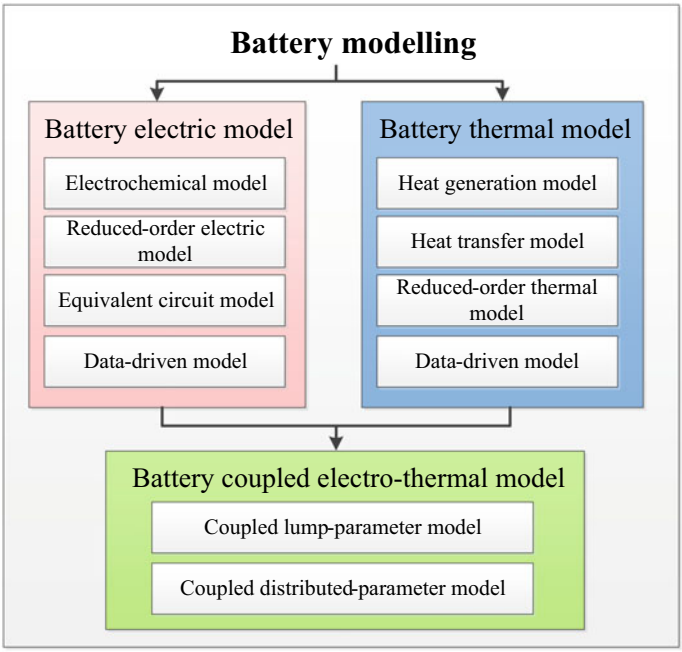

Fig. 4.1 Three typical and widely used battery operation models

4.1.1 Battery Electrical Model

As a fundamental battery operation model, electrical model can be mainly divided into the electrochemical model [2, 3], reduced-order model [4, 5], equivalent circuit model [6, 7] and machine learning model [8–10].

For the electrochemical model of battery, Rahman et al. [2] claim that this type of battery electrical model should own the ability to describe the spatiotemporal dynamics of battery concentration, the electrode potential of each phase, and the Butler–Volmer kinetic for controlling intercalation reactions. Then an electrochemical model is established for describing battery electrochemical behaviours while its parameters are optimized by the particle swarm optimization (PSO) approach. Sung et al. [3] present that the battery electrochemical model is able to provide a highly accurate prediction performance, but it usually needs significant computational efforts for model simulation. Then a model implementation solution is designed to embed this complicated model into the BMS. The main merit of adopting electrochemical model is that a highly accurate description of electrochemical process within a battery could be achieved. However, numerous parameters that reflect battery electrochemistry such as the chemical composition require to be identified by using data science tool, which is actually a big challenge in real battery operation applications. Moreover, many partial differential equations are involved in a

battery electrochemical model, bringing a large computational burden to solve them. It should be known that through making proper assumptions, the full-order electrochemical model could be approximated by the reduced-order model. For instance, after capturing both solid-phase diffusion and electrolyte concentration distribution within battery based on an approximate approach, a simplified physics-based electrochemical model is derived in [4]. Li et al. [5] simplify the electrochemical model with reduced-order to predict discharging capacities of $LiFePO_4$ battery under different conditions. Although some information would inevitably be lost by using the simplified reduced-order model, this type of electrical model would become more desirable for real operation management of battery. Here, the computational effort becomes much lower by using a reduced-order model, while its corresponding parameters could be identified based on the data from measured battery terminal current and voltage.

For the equivalent circuit model of battery, battery electrical dynamics can be captured by using a combination of circuit components including the resistance, capacity, and voltage sources. Due to the simple structure and relatively small amount of parameters need to be identified, equivalent circuit model has become one of the most popular ones for battery real operation management. Figure 4.2 illustrates a classical framework of battery equivalent circuit model with two resistance–capacitance (RC)-networks. Specifically, these RC-networks could reflect battery electrical behaviours such as the charge transfer or diffusion process. Here, the number of RC-networks is generally treated as the order of equivalent circuit model, which requires to be carefully chosen. According to [6], equivalent circuit model with one or two RC-networks could provide satisfactory performance, while higher order of RC-networks becomes unnecessary in many battery operation cases. Nejad et al. [7] provide a critical review for widely adopted equivalent circuit model for Li-ion batteries. Illustrative results indicate that equivalent circuit model with RC-network presents better dynamic performance particular for the prognostics of battery state of charge (SoC) and power.

For the machine learning-based model, various machine learning technologies such as neural networks (NNs) [8, 9] and support vector machine (SVM) [10] have been adopted to derive suitable data science models for capturing battery electrical

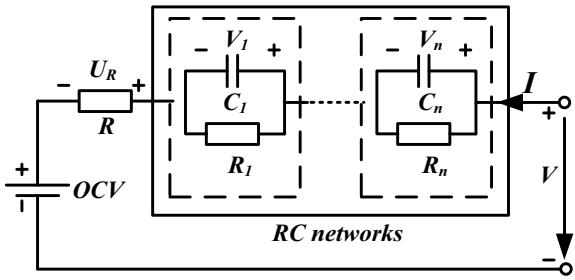

Fig. 4.2 Typical structure of battery equivalent circuit model

dynamics without the requirements of battery prior knowledge. The performance of this type of battery model significantly relies on the experimental data as well as training solutions. To achieve satisfactory prediction accuracy and good generalization performance, experimental data should cover enough battery operation ranges, while the parameters of machine learning models require to be carefully optimized by using suitable training solutions. Moreover, the adaptive data science techniques [11, 12] could be adopted to provide better modelling results.

4.1.2 Battery Thermal Model

Apart from battery electrical dynamics, battery thermal behaviour such as its temperature variation is another key aspect to affect battery operation management because it plays a pivotal role in determining battery performance and service life [13–15]. In this context, different data science models such as heat generation model, heat transfer model, reduced-order thermal model, and machine learning-based model have been proposed to describe battery thermal dynamics. For battery heat generation model, a great deal of solutions are designed to capture battery heat generation, such as activation, concentration, and ohmic loss, which distribute non-uniform within a battery. Three popular ways to assess battery heat generation are described in Eq. (4.1), which have been widely adopted for real battery operation management [16, 17].

$$\begin{cases} Q_a = R \cdot I^2 \\ Q_b = I \cdot (V - \mathrm{OCV}) \\ Q_c = I \cdot (V - \mathrm{OCV}) + I \cdot T \cdot \mathrm{dOCV/d}T \end{cases} \tag{4.1}$$

where R stands for battery internal resistance. I and V represent terminal current and voltage of battery, respectively. OCV means open-circuit voltage of battery. Q_a is the heat generation mainly caused by large currents that across battery internal resistance. Q_b represents heat generation caused by overpotential across RC-networks. Q_c denotes heat generation due to the entropy variation as well as Joule heating.

Besides, for the heat transfer of battery, the convection, conduction, and radiation of heat are the three primary forms within as well as outside a battery [18, 19]. A three-dimensional distributed-parameter heat transfer model is developed by Guo et al. [20] to explore the geometrical currents and heat distribution within a Li-ion battery, as described by,

$$\frac{\partial \rho C_p T_{3C}}{\partial t} = -\nabla(k_{3C} \nabla T_{3C}) + Q \tag{4.2}$$

It can be also expressed by [21],

$$\frac{\partial \rho C_p T_{3C}}{\partial t} = -\frac{\partial}{\partial x}\left(k_x \frac{\partial T_{3C}}{\partial x}\right) - \frac{\partial}{\partial y}\left(k_y \frac{\partial T_{3C}}{\partial y}\right) - \frac{\partial}{\partial z}\left(k_z \frac{\partial T_{3C}}{\partial z}\right) + Q \tag{4.3}$$

where ρ reflects battery density, C_p stands for heat capacity of battery, k_{3C} is a coefficient to reflect battery thermal conductivity (along three dimensions: k_x, k_y, k_z), and Q stands for the heat generation of battery.

Supposing the temperature distribution of a battery within each layer plane is uniform, and only considering one dimension (x, y, z) of battery heat conduction, then a one-dimensional heat conduction thermal model can be simplified as [22],

$$\frac{\partial \rho C_p T_{1C}}{\partial t} = -\frac{\partial}{\partial x}\left(k_x \frac{\partial T_{1C}}{\partial x}\right) + Q \tag{4.4}$$

The three-dimensional heat transfer model is able to describe temperature distribution within a battery, which could be further adopted to detect possible hot spots, especially for high heat generation operations. The one-dimensional heat transfer model is capable of capturing battery temperature gradient along a direction of interest. However, the computational efforts of these heat transfer models are usually too large to be applied in real battery operation management, and they are primarily adopted in offline simulation conditions.

Let heat conduction becomes the only type for heat transfer, heat generation is evenly distributed within a battery, while the temperatures of both battery surface and interior become uniform, then a two-stage battery thermal model [23, 24] that has been widely used in battery operation management is derived as:

$$\begin{cases} C_{q1} \cdot \mathrm{d}T_{\mathrm{in}}/\mathrm{d}t = k_1 \cdot (T_{\mathrm{sh}} - T_{\mathrm{in}}) + Q \\ C_{q2} \cdot \mathrm{d}T_{\mathrm{sh}}/\mathrm{d}t = k_1 \cdot (T_{\mathrm{in}} - T_{\mathrm{sh}}) + k_2 \cdot (T_{\mathrm{amb}} - T_{\mathrm{sh}}) \end{cases} \tag{4.5}$$

where T_{in} is battery internal temperature, while T_{sh} is battery surface temperature; T_{amb} stands for ambient temperature; C_{q1} is battery internal thermal capacity while C_{q2} represents battery surface thermal capacity; k_1 reflects the heat conduction between battery surface and interior, k_2 is the heat conduction between battery surface and ambient temperature.

After defining battery heat generation and transfer parts, numerous battery thermal models with reduced order have been also successfully designed to achieve control purposes for battery operation management [25]. After converting the one-dimensional boundary-value issue into a linear model with low order in the frequency domain, the order of a Li-ion battery thermal model can be decreased, while its temperature prediction could match closely with the results of experiment and three-dimensional finite-element simulations. According to the computational fluid dynamics (CFD) model, a reduced-order state-space thermal model is proposed by using the singular value decomposition method [25], while the similar results as CFD model can be achieved but with much less computational efforts.

4.1.3 Battery Coupled Model

In battery operation applications, there exists strong coupling among different battery dynamics. For example, battery electrical and thermal behaviours are strongly coupled with each other. To better capture battery electrical dynamics (e.g. current, voltage, SoC) and thermal dynamics (e.g. surface and internal temperature), several battery coupled electrothermal models have been proposed, including lump-parameter model and distributed-parameter model [26–28]. For example, a three-dimensional electrothermal model is proposed by Goutam et al. [29] to predict battery SoC and calculate its heat generation. Specifically, this electrothermal model contains a 2D potential distribution model and a 3D temperature distribution model. Then both battery SoC and temperature distribution under constant as well as dynamic currents could be effectively obtained by using this coupled model. In [30], an electrothermal model with decreased order is designed and evaluated by batteries with three different cathode materials. This reduced model is accurate enough for developing quick heating and optimal charging method at low temperature cases. A coupled electrothermal model with three-dimensional is proposed by Basu et al. [31] to analyse the effects of different battery operations such as coolant flow-rates and discharge currents on the variations of battery temperature, further verifying that the contact resistance plays a pivotal role in affecting battery temperature.

4.2 Battery State Estimation

Due to the complex electrochemical characteristics and multi-physics coupling, a trivial emulation of battery operations based on just measured voltage, current, and surface temperature cannot lead to the in-depth understanding or monitoring of operated batteries. In this context, performing accurate estimation of several battery internal states is crucial for advanced battery operation management [32]. This section details the data science-based battery state estimation with a focus on several battery fundamental but important states including the state of charge (SoC), state of power (SoP), state of health (SoH), and joint states estimation.

4.2.1 Battery SoC Estimation

4.2.1.1 Definition of Battery SoC

SoC is a fundamental and critical factor for the operation management of battery, which can be expressed by different formulation forms [33]. SoC generally represents the battery available capacity (C_a) expressed as a percentage of its nominal capacity (C_n) [34]. C_n is the maximum charge amount that can be stored within a battery.

Similar to the fuel vehicle's tank, SoC presents the same functionality as a fuel gauge. Supposing current I is positive and negative for charging and discharging, respectively, a common definition of battery SoC is:

$$\mathrm{SoC}(t) = \mathrm{SoC}(t_0) + \int_{t_0}^{t} \frac{\eta \cdot I(t)}{C_n} \mathrm{d}t \tag{4.6}$$

where $\mathrm{SoC}(t)$ and $\mathrm{SoC}(t_0)$, respectively, denote battery SoC values at time point t and initial time point t_0; η represents coulombic efficiency to reflect the ratio of fully discharged energy to charged energy needed to recover the original capacity.

On the other hand, from the battery electrochemical side, SoC could represent the charge contained in electrode particles. Specifically, the variation of battery SoC is able to reflect the distribution of lithium concentration within electrode particles. Due to the amount of available charge highly relies on the amount of lithium stored in electrodes, SoC can be directly obtained by considering the mean lithium concentration $\overline{C}_s$ as:

$$\mathrm{SoC}(t) = \frac{\overline{C}_s(t) - C_{s,\min}}{C_{s,\max} - C_{s,\min}} \tag{4.7}$$

where $\overline{C}_s(t)$ represents the mean surface Li-ion concentration at time point t, and $C_{s,\min}$ and $C_{s,\max}$ stand for the surface Li-ion concentrations when fully charging and discharging a battery, respectively.

The operation management of battery requires accurate SoC information to indicate the remaining available energy within a battery during its operations. In the laboratory conditions, based upon a known initial SoC value, the referenced battery SoC is generally obtained through a well-controlled coulomb counting approach to accumulate charge transferred [35]. However, complex battery electrochemical dynamics and strongly coupled characteristics make battery SoC is difficult to be measured directly in real-world applications. In this context, reliable battery SoC estimation in real time is a critical part of battery operation management, thus attracting considerable data science research efforts.

4.2.1.2 Data Science-Based SoC Estimation Methods

To date, different data science-based methods were designed to achieve reasonable SoC estimation for battery operation management in the literature. These data science-based methods could be divided into three main categories including the direct calculation method, model-based method, and machine learning method, as shown in Fig. 4.3.

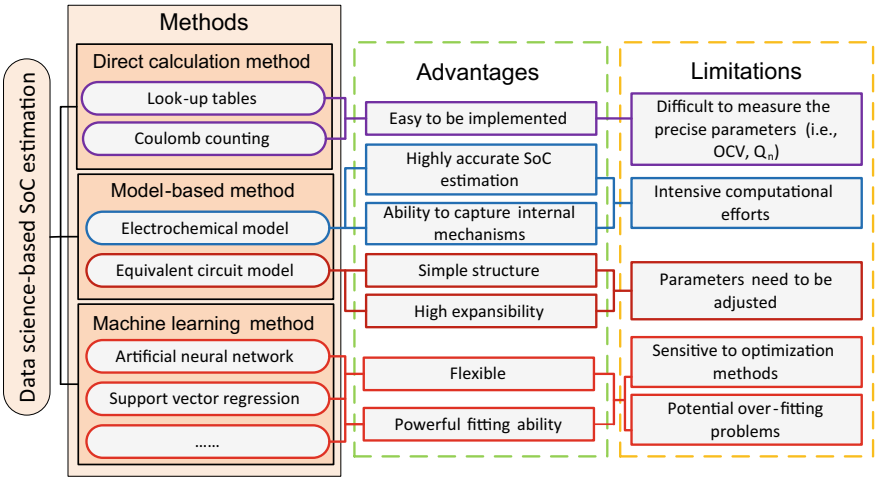

Fig. 4.3 Data science-based battery SoC estimation methods in terms of merits and limitations, reprinted from [32], with permission from Elsevier

For data science direct calculation method, two common solutions are noteworthy. First, as there exist obvious mapping relations between battery SoC and some battery direct factors such as the open-circuit voltage (OCV) and impedance, after obtaining the data of these battery factors, the battery SoC could be inferred by the predefined lookup tables that describe such a relation [36]. Besides, based upon the obtained data of battery nominal capacity and exact current profiles, the variation of battery SoC could be conveniently obtained by the coulomb counting approach. One obvious superiority of these two methods is the easy way to be implemented for battery SoC estimation. However, as battery capacity would inevitably vary with different ageing levels, and OCV needs to be obtained after a rest period, precisely online measuring these data is still a daunting challenge during battery operation management. In the light of this, attempts have been made to estimate battery SoC through other data science supporters such as model-based methods.

For the model-based method, according to a proper model such as dynamics equations, different estimation strategies together with easily collect current or voltage data would be employed to estimate battery SoC. One popular model type is the battery electrochemical model (EM) as battery internal mechanisms such as kinetic and charge transfers within a battery could be described by it, further leading to an accurate SoC estimation of battery. However, as EM-based methods involve many parameters and partial differential equations, it generally requires a large computational burden to implement them. In order to facilitate a real-time application, suitable simplifications are always required. Another widely used model type is the battery equivalent circuit model (ECM) which adopts electrical circuit components to emulate battery dynamics. Due to a relatively simple structure and reasonable expansibility, ECM becomes a promising tool for battery real-time SoC estimation. However, considering the ECMs' parameters would vary over time, using

the invariant parameters under different temperature, SoC or ageing levels could cause large estimation error [37]. Great efforts are required to periodically recalibrate ECMs' parameters, further ensuring their extensibility. Besides, after obtaining different battery data in real applications, it is vital to develop proper solutions such as the joint parameter/SoC estimation tool for adjusting model parameters adaptively.

The machine learning method, free of understanding battery electrochemical mechanisms, has also been widely adopted to estimate battery SoC. Due to the potential merits such as being flexible and highly nonlinear fitting ability, various techniques including the neural network (NN) [38] and support vector machine (SVM) [39] have been utilized to estimate battery SoC. However, these data science solutions are very sensitive to their optimization strategies and the quality of collected data. In addition, overfitting issues would happen if improper training modes are utilized.

4.2.1.3 Case Study: Battery SoC Estimation with RLS and EKF

In this subsection, we will introduce a data science-based SoC estimation method for Li-ion battery with recursive least square (RLS) and extended Kalman filter (EKF). As the most widely used model-based method, the RLS-EKF integrates the RLS-based online model identification and the EKF-based SoC observation in a dual sequential framework.

The estimation accuracy of this method largely depends on the accuracy of the model. However, a model with a higher accuracy requires more parameters to be identified, that is to say, a higher computational cost is required. Generally, a battery model suitable for the real-time application has a simple topology while capturing the major dynamics of Li-ion battery. In the light of this, this case study uses the Thevenin model to verify the RLS-EKF algorithm. As is shown in Fig. 4.4, R_0 is the ohmic resistance. The single RC branch is used to simulate the polarization effects due to passivation layers on the electrodes, charge transfer between electrode and electrolyte, diffusion, migration, and convection processes. The dynamics of the Thevenin model in use is written as:

$$\begin{cases} U_t(t) = U_{\mathrm{OCV}}(\mathrm{SoC}(t)) - i(t)R_0 - U_1(t) \\ \dot{U}_1(t) = -\frac{U_1(t)}{R_1C_1} + \frac{i(t)}{C_1} \end{cases} \tag{4.8}$$

Further discretizing the above formula can obtain:

$$\begin{cases} U_t(k) = U_{\mathrm{OCV}}(\mathrm{SoC}(k)) - i(k)R_0 - U_1(k) \\ U_1(k+1) = e^{-\frac{\Delta t}{R_1C_1}}U_1(k) + R_1(1 - e^{-\frac{\Delta t}{R_1C_1}})i(k) \end{cases} \tag{4.9}$$

The OCV is a nonlinear function of SoC which should be calibrated accurately to adopt the model-based estimation. In order to identify the functional relationship between OCV-SoC, it is necessary to obtain the OCV-SoC curve through the OCV experiment, fit the experimental curve through the empirical function, identify the

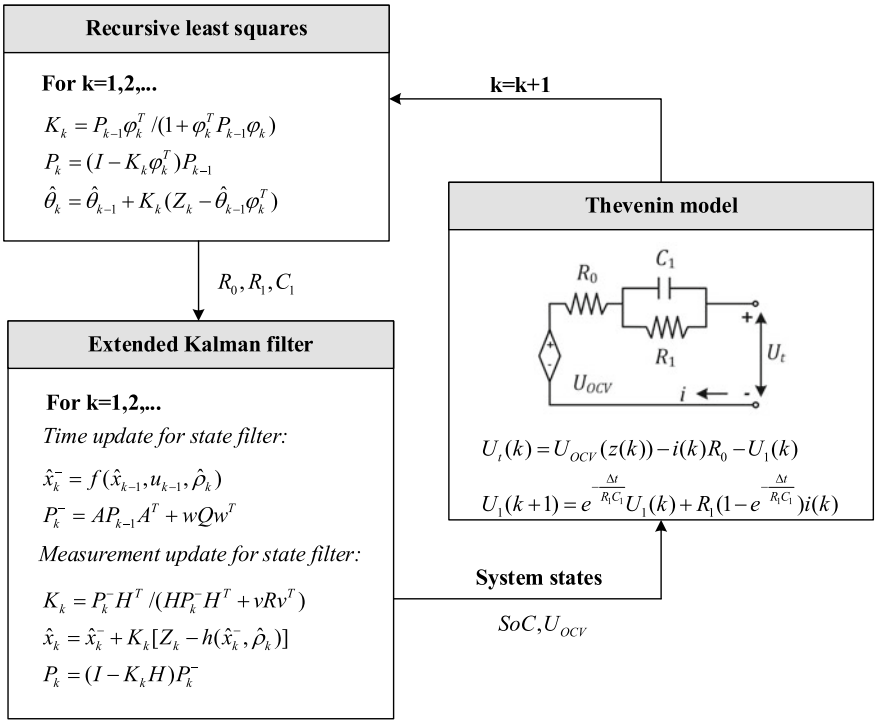

Fig. 4.4 Data science-based battery SoC estimation method with RLS and EKF

parameters of the given function through the parameter identification method, and finally get the OCV-SoC function relationship. It is usually possible to use higher-order polynomial approximation as:

$$U_{\mathrm{OCV}}(z) = k_0 + k_1 z + k_2 z^2 + \cdots + k_n z^n \tag{4.10}$$

where z denotes the SoC, k_n $(n = 1, 2, \ldots, n_f)$ are the polynomial coefficients, and n_f is the polynomial order which is selected to be 5 in this case.

Since the sampling of current and voltage signals is discrete in the actual battery system, the continuous-time model of SoC should also be discretized:

$$\mathrm{SoC}(k+1) = \mathrm{SoC}(k) - \eta\frac{i(k)\Delta t}{Q} \tag{4.11}$$

The adoption of RLS-based online model identification necessitates formulating a regression model. To achieve this, a new variable is defined as:

$$\frac{U_t(s) - U_{\mathrm{OCV}}(s)}{i(s)} = \left(-R_0 + \frac{R_1}{1 + R_1C_1s}\right) \tag{4.12}$$

By applying the bilinear transform, Eq. (4.12) can be transformed to:

$$\frac{U_t(z) - U_{\mathrm{OCV}}(z)}{i(z)} = \frac{c_2 + c_3}{1 - c_1 z^{-1}} \tag{4.13}$$

where

$$\begin{aligned} c_1 &= \frac{2R_1C_1 - \Delta t}{2R_1C_1 + \Delta t} \\ c_2 &= \frac{(R_0 + R_1)\Delta t + 2R_0R_1C_1}{-(\Delta t + 2R_1C_1)} \\ c_3 &= \frac{(R_0 + R_1)\Delta t - 2R_0R_1C_1}{-(\Delta t + 2R_1C_1)} \end{aligned}$$

Then the discrete-time expression of the system can be written as:

$$U_{q,k} = \theta_k \phi_k^T \tag{4.14}$$

where $U_{q,k} = U_{t,k}$, $\theta_k = [(1 - c_1)U_{\mathrm{OC},k}, c_1, c_2, c_3]$, $\phi_k = [1, U_{t,k-1}, i_k, i_{k-1}]$. The regression model is then identifiable with the RLS method. A forgetting factor (λ) is used to give more weight to the recently obtained data while discounting the contribution of historical data. Once the model parameters are obtained, the system states including polarization voltage and SoC are estimated by using EKF. Choose SoC and U_1 as the state variable, electric current as input quantity, and terminal voltage (U_t) as output quantity. The equation can be transformed as:

$$\begin{cases} \begin{bmatrix} U_1(k) \\ \mathrm{SoC}(k) \end{bmatrix} = \begin{bmatrix} e^{\left(-\frac{\Delta t}{R_1C_1}\right)} & 0 \\ 0 & 1 \end{bmatrix} \begin{bmatrix} U_1(k-1) \\ \mathrm{SoC}(k-1) \end{bmatrix} + \begin{bmatrix} R_1\left(1 - e^{\left(-\frac{\Delta t}{R_1C_1}\right)}\right) \\ -\eta \Delta t / Q_N \end{bmatrix} i(k-1) \\ \qquad\qquad + w_{k-1} \\ U_t(k) = f[\mathrm{SoC}(k)] - U_1(k) + R_0 i(k) + v_k \end{cases} \tag{4.15}$$

where w_{k-1} is the random process noise sequence, and v_k is the random observation noise sequence. Since $f[\mathrm{SoC}(k)]$ is nonlinear with respect to SoC, the formula is expanded into a Taylor series around the optimal prediction estimate to linearize. The RLS-based model identification and EKF-based SoC estimation are integrated in a dual sequential framework as shown in Fig. 4.4.

In this case, A123 ANR26650 M1-B batteries with a nominal capacity of 2.5 Ah are selected to verify the algorithm performance. In order to obtain the maximum usable capacity of the battery, a constant volume experiment must be carried out at a room temperature of 25 °C. In detail, a constant-current-constant-voltage method with 1C rate is used to charge the batteries until the voltage reaches 3.6 V and

then current drops to 0.05C. A constant-current method with 1C rate is used to discharge cells until the voltage drops to 2.0 V. The battery OCV has a monotonic mapping relationship with the SoC. Determining the OCV-SoC mapping rule is of great significance for improving the accuracy of battery modelling and SoC state estimation. Therefore, after the constant volume test, it is necessary to calibrate the OCV-SoC curve. Specifically, taking the charging OCV as an example, if 10% SoC point is used as the test point, battery is discharged to the cut-off voltage 2.75 V with a 1C current at a constant current, and then left for 2 h as the voltage of SoC = 0%. 1C rate is utilized to charge the battery in cross-current. The cut-off condition is that the charging time reaches 6 min, and after 2 h left, the terminal voltage is recorded as the OCV corresponding to the current SoC, and so on, recording 10%, 20%, …, 90% OCV. The ECM shown in Fig. 4.4 is built by using MATLAB Simulink. The model parameters are all defined according to the battery testing result. An enhanced UDDS, DST, and FUDS profile shown in Fig. 4.5 is used to verify the feasibility of RLS and EKF algorithms.

As shown in Fig. 4.6, the blue line is the real SoC value, and the red line is the SoC value estimated by the RLS-EKF algorithm. The RMSE and the MAE under different working conditions are shown in Table 4.1.

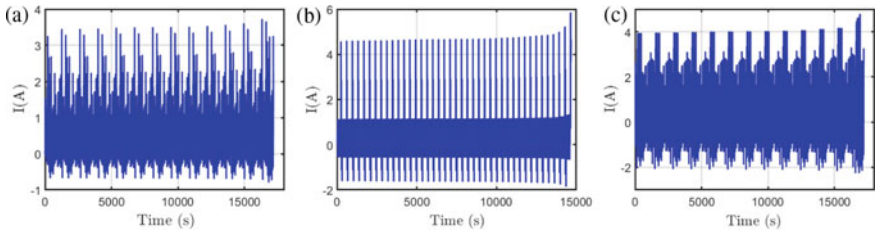

Fig. 4.5 Load profile for testing: **a** an enhanced UDDS profile; **b** an enhanced DST profile; **c** an enhanced FUDS profile

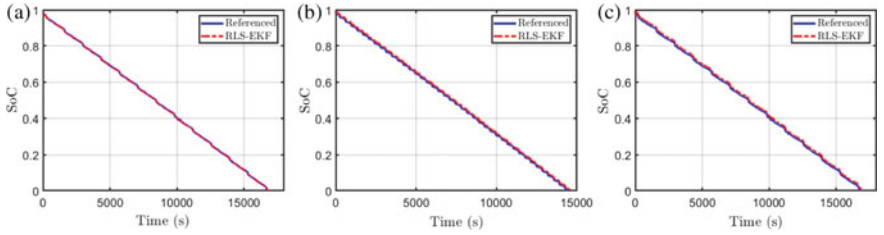

Fig. 4.6 SoC estimation result: **a** UDDS; **b** DST; **c** FUDS

Table 4.1 Performance of RLS-EKF under different working conditions

	UDDS (%)	DST (%)	FUDS (%)
RMSE	0.27	0.87	1.04
MAE	0.75	1.23	1.33

4.2.2 Battery SoP Estimation

4.2.2.1 Definition of Battery SoP

State of power (SoP) is another critical factor for battery operation management and usually utilized to reflect the available power that a battery could supply or absorb over a short time horizon [40]. In theory, battery SoP could be viewed as a result of threshold current and responded voltage, while different operation constraints also need to be explicitly considered. Supposing that discharging power is positive while charging power is negative, battery SoP can be generally expressed by [41]:

$$\begin{cases} \mathrm{SoP}^c(t) = \max\left(P_{\min}, V(t+\Delta t)\cdot I^c_{\min}\right) \\ \mathrm{SoP}^d(t) = \min\left(P_{\max}, V(t+\Delta t)\cdot I^d_{\max}\right) \\ \text{Subject to operation constraints} \end{cases} \tag{4.16}$$

where $\mathrm{SoP}^c(t)$ and $\mathrm{SoP}^d(t)$ denote battery charging and discharging SoPs at time point t, respectively, $P_{\min}$ and $P_{\max}$ represent the minimum and maximum limitations of battery power, Δt is the specific future time period, $V(t+\Delta t)$ stands for battery terminal voltage at time point $t+\Delta t$, and $I^c_{\min}$ and $I^d_{\max}$ are minimum continuous charging current as well as maximum continuous discharging current from time point t to $t+\Delta t$, respectively. $I^c_{\min}$ and $I^d_{\max}$ require to be obtained under the cases of battery operation constraints are not exceeded. These operation constraints usually contain battery voltage, current, SoC, and sometimes temperature.

For the simulation applications, battery SoP reference is generally obtained by the high-fidelity battery model with the consideration of different operation constraints [42]. In the laboratory conditions, battery SoP could be decided through well-designed pulse tests with the consideration of some modified current rate and duration time. For real EV applications, due to the energy-flow management such as the power split and battery charging during regenerative braking highly depends on the available power of battery, reliable battery SoP estimation could benefit not only the regulation of vehicular power flow but also the optimization of overall powertrain efficiency. Moreover, for battery itself, knowing its future SoP could benefit fast charging mode and battery performance. In this context, it is vital to design effective data science strategy for reliable battery SoP estimation that takes the highly nonlinear dynamics and different operation constraints of battery into account.

4.2.2.2 Data Science-Based SoP Estimation Methods

Battery SoP estimation studies are relatively scarce compared with battery SoC estimation methods involving a plethora of research. According to a systematic review in [40], data science-based SoP estimation methods can be mainly divided into two categories, as shown in Fig. 4.7.

For characteristic map (CtM)-based method, a static interdependence between battery SoP and other state variables such as SoC, temperature, voltage, and power pulse duration is established offline. To further enhance the estimation performance of CtM-based method, the difference between measured battery power and estimated SoP value is calculated. Then the reference points within CtM could be adapted in the conditions of a huge deviation that appears [43]. CtM-based method could be readily implemented, owing to its straightforward treatment. However, several issues are still not addressed thoroughly: First, past and current battery information is difficult to be considered in CtMs. As battery power dynamics strongly relies on its operation condition, the accuracy of battery SoP estimation will be thus influenced severely. Second, in order to construct a high-performance CtM under different battery operating conditions, a large amount of information requires to be stored by the multi-dimensional forms, further leading to a large computational burden on the micro-controller. In this context, the online SoP estimation method through deriving suitable battery model with various computational levels is explored and exploited.

For model-based approach, ECM and its variants are usually adopted to estimate battery SoP. After formulating ECM with a discrete-time state-space form, various solutions such as Kalman filter [44] and least square-based approach [42] have been adopted to derive reasonable SoP estimators. To guarantee the estimation accuracy of SoP, an ECM that could not only describe battery overall dynamics but also presents proper structure and parameters becomes necessary. In this context,

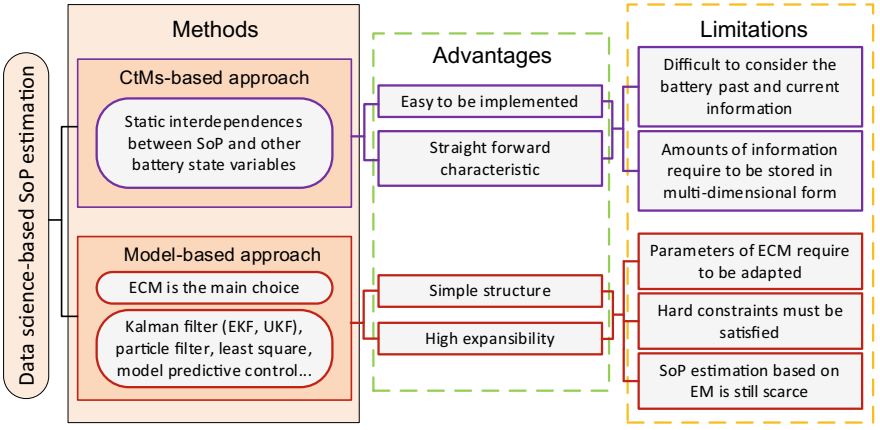

Fig. 4.7 Data science-based battery SoP estimation methods in terms of merits and limitations, reprinted from [32], with permission from Elsevier

ECM's parameters need to be adapted under real-time data from different operating SoC, temperature, and ageing states. In addition, to ensure battery operated safely, the operating constraints of current, voltage, SoC, and/or even internal temperature are required to be satisfied during battery SoP estimation. In addition, ECM-based approach is difficult to depict battery's inside electrochemical process, further leading to poor generalization. Unfortunately, EM-based approach is still scarce in battery SoP estimation domain.

4.2.2.3 Case Study: Battery SoP Estimation with Multi-constrained Dynamic Method

In this subsection, we will introduce a data science-based SoP estimation method for Li-ion battery with the multi-constrained dynamic method. This method comprehensively considers multiple constraint variables, such as terminal voltage, current, SoC, etc., to predict battery SoP in real-time. At the same time, the influence of dynamic response characteristics such as electrochemical kinetics, thermodynamics, and hysteresis effects on the SoP prediction results are comprehensively considered.

As mentioned above, the peak power capability of Li-ion battery is affected by the maximum charge and discharge current, the maximum and minimum cut-off voltage, the remaining available capacity of the battery, etc. In order to estimate the peak power capability accurately, there are multiple constraints (voltage, current, SoC, rated power) that should be taken into consideration, which can be expressed as follows:

$$\begin{cases} U_{\min} < U < U_{\max} \\ I_{\min}^{\text{chg}} < I < I_{\max}^{\text{dis}} \\ \text{SoC}_{\min} < \text{SoC} < \text{SoC}_{\max} \\ P_{\min}^{\text{chg}} < P < P_{\max}^{\text{dis}} \end{cases} \tag{4.17}$$

where U, I, SoC, P represent the battery's terminal voltage, current, SoC, and power. For the battery charge and discharge process, the peak power capability of Li-ion battery can be calculated as follows:

$$\begin{cases} P_{\min}^{\text{chg}} = \max(P_{\min}, \text{UI}) \\ P_{\max}^{\text{dis}} = \min(P_{\max}, \text{UI}) \end{cases} \tag{4.18}$$

Further, the maximum discharge current and minimum charge current of the battery need to meet the following conditions:

$$\begin{cases} I_{\min}^{\text{chg}} = \max(I_{\min}, I_{\min}^{\text{chg},U}, I_{\min}^{\text{chg},SoC}) \\ I_{\max}^{\text{dis}} = \min(I_{\max}, I_{\max}^{\text{dis},U}, I_{\max}^{\text{dis},SoC}) \end{cases} \tag{4.19}$$

Based on the combination of the three constraints, the peak power capability of the battery is finally expressed as follows:

$$\begin{cases} P_{\min}^{\text{chg}} = \max(P_{\min}, P_{\min}^{\text{chg},U}, P_{\min}^{\text{chg},C}, P_{\min}^{\text{chg,SoC}}) \\ P_{\max}^{\text{dis}} = \min(P_{\max}, P_{\max}^{\text{dis},U}, P_{\max}^{\text{dis},C}, P_{\max}^{\text{dis,SoC}}) \end{cases} \Rightarrow \begin{cases} P_{\min}^{\text{chg}} = \max(P_{\min}, U(I_{\min}^{\text{chg}})I_{\min}^{\text{chg}}) \\ P_{\max}^{\text{dis}} = \min(P_{\max}, U(I_{\max}^{\text{dis}})I_{\max}^{\text{dis}}) \end{cases} \tag{4.20}$$

This case continues to use Thevenin equivalent circuit model to estimate SoP. Similarly, A123 ANR26650 M1-B batteries with a nominal capacity of 2.5 Ah are used to verify the multi-constraint algorithm. In particular, by consulting the battery's user manual, it is necessary to pay attention to the battery-related limit parameters. As shown in Table 4.2, the parameters that need to be paid attention to in SoP estimation are listed. The discharge current is artificially specified as positive.

An enhanced DST profile shown in Fig. 4.8a is used to verify the algorithms. In order to accurately obtain the peak current under the SoC constraint, the RLS-EKF algorithm is first used to estimate battery SoC. Parameter identification and SoC estimation have been introduced in detail in Sect. 4.2.1.3 and will not be repeated here. As shown in Fig. 4.8b, the root-mean-square error (RMSE) is 0.87%, while the mean-absolute error (MAE) is 1.23%.

Next, derive detailed expressions of peak discharge and charge currents under SOC and voltage constraints. The load current is assumed to be constant between the k sampling time and the $(k + L)$ sampling time, where L represents the prediction time horizon. Under the excitation of peak discharge current, the terminal voltage would drop to the lower cut-off voltage, so that the following equation can be drawn:

Table 4.2 Upper and lower cut-off thresholds for SoC, voltage, and current

	SoC (%)	Voltage (V)	Current (A)
Maximum	96	3.6	120
Minimum	5	2	−25

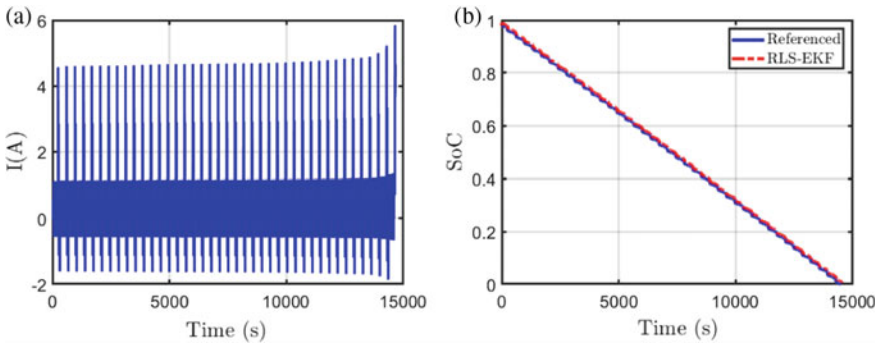

Fig. 4.8 SoC estimation: **a** an enhanced DST profile; **b** SoC estimation results

$$U_{t,\min} = U_{\mathrm{OCV}}(k+L) - U_1(k+L) - I_{L,\max}^{\mathrm{dis,volt}} R_0 \tag{4.21}$$

The polarization voltage at the $(k+L)$ can be expressed with the battery model as:

$$U_1(k+L) = e^{\frac{-L\Delta t}{R_1 C_1}} U_1(k) + (1 - e^{\frac{-L\Delta t}{R_1 C_1}}) R_1 \sum_{j=1}^{L} e^{\frac{-(j-1)\Delta t}{R_1 C_1}} I_{L,\max}^{\mathrm{dis,volt}} \tag{4.22}$$

In order to derive $U_{\mathrm{OCV}}(k+L)$, the SoC recurrent relationship is defined as:

$$\mathrm{SoC}(k+L) = \mathrm{SoC}(k) - \frac{\eta I_{L,\max}^{\mathrm{dis,volt}} L\Delta t}{Q} \tag{4.23}$$

So that,

$$\begin{aligned} U_{\mathrm{OCV}}(k+L) &= U_{\mathrm{OCV}}(k)\left(\mathrm{SoC}(k) - \frac{\eta I_{L,\max}^{\mathrm{dis,volt}} L\Delta t}{Q}\right) \\ &\approx U_{\mathrm{OCV}}(k) - \frac{\eta I_{L,\max}^{\mathrm{dis,volt}} L\Delta t}{Q} \frac{\partial U_{\mathrm{OCV}}}{\partial \mathrm{SoC}}_{\mathrm{SoC}(k)} \end{aligned} \tag{4.24}$$

The final expression of the voltage-constrained peak discharge current is:

$$I_{L,\max}^{\mathrm{dis,volt}}(k) = \frac{U_{\mathrm{OCV}}(k) - e^{\frac{-L\Delta t}{R_1 C_1}} U_1(k) - U_{t,\min}}{\frac{\eta L\Delta t}{Q} \frac{\partial U_{\mathrm{OCV}}}{\partial \mathrm{SoC}}_{\mathrm{SoC}(k)} + \left(1 - e^{\frac{-L\Delta t}{R_1 C_1}}\right) R_1 \sum_{j=1}^{L} e^{\frac{-(j-1)\Delta t}{R_1 C_1}} + R_0} \tag{4.25}$$

The voltage-constrained peak charge current is:

$$I_{L,\min}^{\mathrm{dis,volt}}(k) = \frac{U_{\mathrm{OCV}}(k) - e^{\frac{-L\Delta t}{R_1 C_1}} U_1(k) - U_{t,\max}}{\frac{\eta L\Delta t}{Q} \frac{\partial U_{\mathrm{OCV}}}{\partial \mathrm{SoC}}_{\mathrm{SoC}(k)} + \left(1 - e^{\frac{-L\Delta t}{R_1 C_1}}\right) R_1 \sum_{j=1}^{L} e^{\frac{-(j-1)\Delta t}{R_1 C_1}} + R_0} \tag{4.26}$$

SoC has to be maintained within a certain range to improve the battery's efficiency and extend the calendar life. The peak discharge and charge current constrained by SoC limit can be derived as:

$$\begin{cases} I_{L,\max}^{\mathrm{dis,SoC}}(k) = \frac{Q(\mathrm{SoC}(k) - \mathrm{SoC}_{\min})}{\eta L\Delta t} \\ I_{L,\max}^{\mathrm{chg,SoC}}(k) = \frac{Q(\mathrm{SoC}(k) - \mathrm{SoC}_{\max})}{\eta L\Delta t} \end{cases} \tag{4.27}$$

So that multi-constrained peak discharge and charge currents are:

$$\begin{cases} I_{L,\max}^{\text{dis}}(k) = \min\left\{I_{L,\max}^{\text{dis,volt}}(k), I_{L,\max}^{\text{dis,SoC}}(k), I_{L,\max}^{\text{dis,current}}(k)\right\} \\ I_{L,\min}^{\text{chg}}(k) = \max\left\{I_{L,\min}^{\text{chg,volt}}(k), I_{L,\min}^{\text{chg,SoC}}(k), I_{L,\min}^{\text{chg,current}}(k)\right\} \end{cases} \tag{4.28}$$

After the peak discharge/charge current is determined, the discharge/charge voltage during the prediction time horizon can be derived as:

$$\begin{cases} U_t(k+i) = U_{\text{OCV}}(k) - e^{\frac{-i\Delta t}{R_1C_1}}U_1(k) \\ \quad -\left[\frac{\eta i\Delta t}{Q}\frac{\partial U_{\text{OCV}}}{\partial \text{SoC}}_{\text{SoC}(k)} + (1-e^{\frac{-\Delta t}{R_1C_1}})R_1\sum_{j=1}^{i}e^{\frac{-(j-1)\Delta t}{R_1C_1}} + R_0\right]I_{L,\max}^{\text{dis}}(k) \\ U_t(k+i) = U_{\text{OCV}}(k) - e^{\frac{-i\Delta t}{R_1C_1}}U_1(k) \\ \quad -\left[\frac{\eta i\Delta t}{Q}\frac{\partial U_{\text{OCV}}}{\partial \text{SoC}}_{\text{SoC}(k)} + (1-e^{\frac{-\Delta t}{R_1C_1}})R_1\sum_{j=1}^{i}e^{\frac{-(j-1)\Delta t}{R_1C_1}} + R_0\right]I_{L,\max}^{\text{chg}}(k) \end{cases} \tag{4.29}$$

Based on the above derivations, the power sequence under the peak current for the whole prediction time horizon can be expressed as:

$$\begin{cases} P_{\text{dis}}(k+i) = I_{L,\max}^{\text{dis}}(k)U_t(k+i) \\ P_{\text{chg}}(k+i) = I_{L,\min}^{\text{chg}}(k)U_t(k+i) \end{cases} \tag{4.30}$$

where $i = 1, 2, \ldots, L$.

And the final expression of peak power with multi-constrained algorithm can be drawn as:

$$\begin{cases} P_{\text{peak}}^{\text{dis}}(k) = \min\limits_{i=1,2,\ldots,L}[P_{\text{dis}}(k+i)] \\ P_{\text{peak}}^{\text{chg}}(k) = \max\limits_{i=1,2,\ldots,L}[P_{\text{chg}}(k+i)] \end{cases} \tag{4.31}$$

Here, this case choose the charging and discharging time as 10 s to verify the multi-constraint algorithm. As shown in Fig. 4.9, the change curve of peak charge and discharge current value under different constraint conditions (voltage, SoC, and current) and the change curve of peak charge and discharge current value under multiple constraint conditions are given.

According to the value of the above-mentioned current, the terminal voltage is further calculated, and then the peak charge–discharge common rate is calculated. The result of SoP estimation is shown in Fig. 4.10.

4.2.3 Battery SoH Estimation

4.2.3.1 Definition of Battery SoH

Battery would inevitably experience gradual performance fading during its lifetime, owing to its side reaction [45]. In general, battery SoH could be described by its

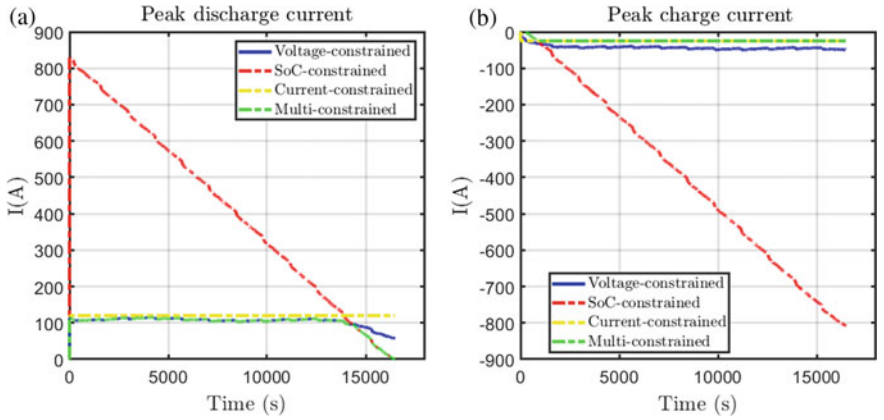

Fig. 4.9 **a** Peak discharge current; **b** peak charge current

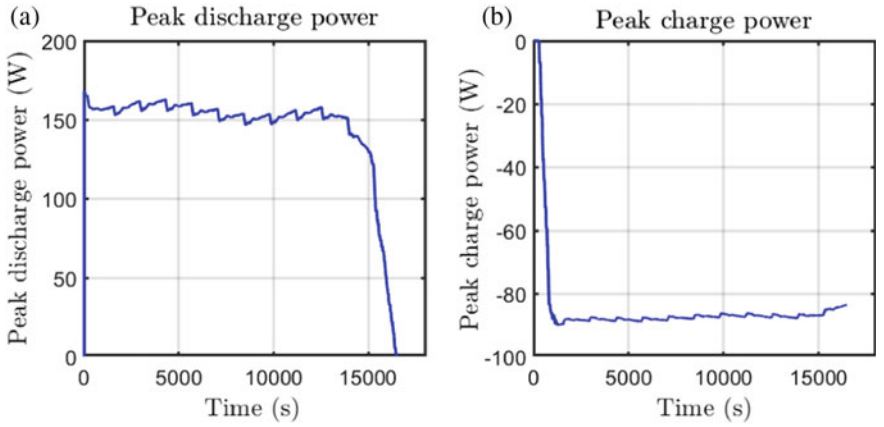

Fig. 4.10 SoP estimation results: **a** peak discharge power; **b** peak charge power

capacity or internal resistance status as:

$$\begin{cases} \mathrm{SoH}_C = \frac{C_a}{C_n} \times 100\% \\ \mathrm{SoH}_R = \frac{R_a - R_r}{R_r} \times 100\% \end{cases} \tag{4.32}$$

where C_a denotes battery actual capacity and C_n is the nominal capacity, and R_a reflects battery actual internal resistance and R_r is the rated internal resistance.

In real applications such as EVs, a 20% capacity degradation and 100% internal resistance increase are generally considered as the end-of-life (EoL) of a battery. In this context, SoH becomes a key factor to underline effective, safe operation management of battery [46]. As it is difficult to directly measure battery capacity and

internal resistance with commercially available sensors in real applications, online battery SoH estimation based on the low-cost suite of sensors is crucial for obtaining accurate battery SoH information.

4.2.3.2 Data Science-Based SoH Estimation Methods

A great deal of efforts based on data science techniques has been done for battery SoH estimation, which could be roughly divided into four categories including the physics-based model, empirical model, differential voltage analysis (DVA)/incremental capacity analysis (ICA)-based method [47], and machine learning method. A schematic of available data science-based battery SoH estimation methods is illustrated in Fig. 4.11. Physics-based model adopts partial differential equations (PDEs) to describe battery dynamics of internal physicochemical reactions that are highly related to battery ageing dynamics. This type of model is able to provide clear physical meaning and highly accurate performance. Nevertheless, it faces some challenges in terms of simplifying model and identifying its numerous parameters before it can be fully eligible for real-time implementations [48].

For the empirical model-based approach, after fitting battery degradation data under specific conditions, it could present a light computational burden and provide acceptable SoH estimation accuracy when a battery is operated under similar conditions as the training case [49]. In general, systematical battery degradation tests with laborious and time-consumed efforts require to be performed for establishing an empirical model for SoH estimation. Besides, a derived empirical model would exhibit a poor robustness to the unseen operating conditions and bad generalization

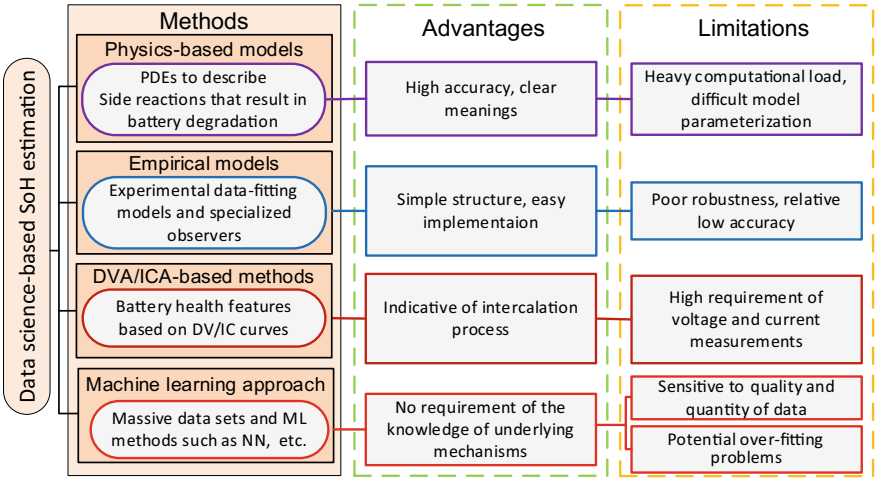

Fig. 4.11 Data science-based battery SoH estimation methods in terms of merits and limitations, reprinted from [32], with permission from Elsevier

ability to batteries with different chemistry or even the dis-similar batch of same chemistry. Therefore, regular model recalibration is vital to increase the related time and cost for developing model. On the other hand, with the rapid development of advanced embedded systems with light computation effort, the physics-based SoH estimation method could be utilized in real battery operation management in future. Then the corresponding simplification and parameterization solutions could become a focus in this direction.

Besides, ICA is also an efficient data science tool to estimate battery SoH [50]. According to the differentiation of charged capacity over battery voltage in the conditions of constant-current charging, the voltage plateaus on battery voltage curve could be transformed into easily identifiable peaks of the IC curve. In this context, the peak position, amplitude, and envelope area of IC curves at different cycles could be utilized to estimate battery SoH [51]. Through using the signal filtering technologies to procure smooth IC curves, the SoH estimation result can be compromised as the peak amplitude is significantly sensitive to the measurement noise. In addition, the voltage range of the voltage curve should cover the voltage corresponding to the peak of the IC curve, which may reduce its feasibility in actual implementation.

Due to the superiority of the mechanism-free nature, advanced machine learning methods such as support vector machine (SVM) and Gaussian process regression (GPR) also become popular for battery SoH estimation [52]. First, a professional battery test that includes all SOH impact factors is carried out, and then the battery SOH model will be synthesized through using machine learning to map these impact factors to the battery SOH. However, the effectiveness of machine learning-based methods largely depends on both the quality and quantity of test data, and the derived models are often affected by the intensity of heavy calculations.

4.2.3.3 Case Study: Battery SoH Estimation with Optimized Partial Voltage Profile

In this subsection, we will introduce a data science-based SoH estimation method for Li-ion battery with optimized partial charging voltage profiles [53]. With a certain amount of dataset from the battery cells, non-dominated sorting genetic algorithm II (NSGA-II) is applied to automatically select the optimal multiple voltage ranges for battery SoH estimation. We can then directly calculate the battery capacity according to the optimized charging voltage profiles.

Normally, the discharging profile of the battery is determined by the load. The charging profile is usually a constant-current constant-voltage (CCCV) process, which is a relatively fixed procedure. Thus, the partial voltage profiles are selected to derive the SoH information in the proposed method.

The battery SoC is defined as,

$$\mathrm{SoC} = \frac{Q_t}{Q_{\mathrm{av}}} \times 100\% \tag{4.33}$$

where Q_t is the energy left in the battery, and Q_{av} is the maximum available battery capacity at present. The energy left can be known by the integration of the current flowing in and out of the battery. Thus, we can obtain the Coulomb counting equation as follows,

$$\text{SoC}(k+1) = \text{SoC}(k) + \frac{\eta \cdot I(k) \cdot T_s}{Q_{\text{av}}} \tag{4.34}$$

where T_s is the sampling interval. Considering that the Coulombic efficiency is usually above 99.6% for $LiFePO_4$ battery and NMC cell, η is defined as 100% in the rest of the derivation.

According to Eq. (4.34), the following equation can be obtained,

$$Q_{\text{av}} = \frac{\sum_{k=A_1}^{A_2} \eta \cdot I(k) \cdot T_s}{\text{SoC}(A_1) - \text{SoC}(A_2)} \tag{4.35}$$

where A_1 and A_2 are the start and termination of the partial voltage profile, respectively.

Generally, the voltage and current are always monitored by a battery management system to ensure the safety of the battery during battery operation management process. It is possible to find a specific voltage ranges from the battery charging process for SoH estimation. Figure 4.12 shows the voltage curve of an NMC-based battery during the charging process. Thus, if the current between U_{A_1} and U_{A_2} is integrated as $\sum_{k=A_1}^{A_2} \eta \cdot I(k) \cdot T_s$ and the SoC variation $(\text{SoC}(A_1) - \text{SoC}(A_2))$ has already known, the battery capacity can be directly calculated from Eq. (4.35).

Now, we can deduce that a proper voltage range $(U_{A_1} \sim U_{A_2})$ should be chosen before estimating the battery SoH during the degradation process. From [53], we know that arbitrarily choosing a voltage profile may not always receive the same good accuracy for SoH estimation. Therefore, it is critical to select the optimal voltage range of the battery capacity prediction when Eq. (4.35) is used. In addition,

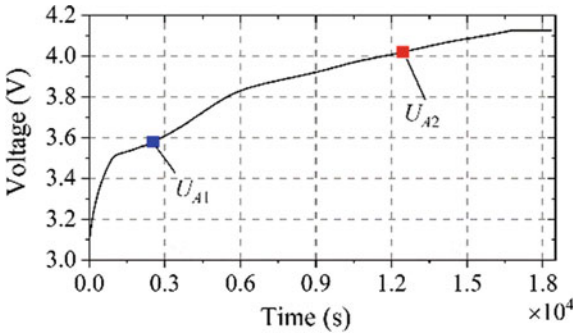

Fig. 4.12 Voltage charge curve of NMC battery, reprinted from [53], with permission from Elsevier

the partial voltage range is also easier to be obtained in the daily usage of the EV compared with the full voltage charging profile. The proposed method is able to effectively compute the Li-ion battery SoH online during the EV charging process.

In this subsection, we plan to propose a methodology to find the optimal voltage range for the battery SoH estimation with data science technique. A single voltage range is firstly considered to predict the battery capacity. Grid search is proposed to optimize a single voltage range with best prediction accuracy. MSE is used to evaluate the accuracy of the estimation and act as the objective function for the grid search optimization. Grid search is an exhaustive searching algorithm, which can select the optimal single voltage range as illustrated in Fig. 4.13. Grid search starts from point A_s and ends at point A_e, the minimal step is $S_{\min}$, and the maximal step is defined as $L_{\max}$. Based on the above definitions, the entire charging voltage curve can be divided into pieces. In this way, grid search can evaluate all the voltage segments and their combinations. The iteration of the grid search will not stop until all the possible voltage ranges are crossed.

Three NMC batteries designed for a market available EV are used to validate the proposed method. The nominal capacity is 63 Ah, and the nominal voltage is 3.7 V, and the voltage ranges from 3 to 4.15 V. The three NMC batteries are aged at accelerated calendar ageing condition illustrated in Table 4.3. The cells are stored in the thermostat at 35, 40 and 45 °C, while the SoC is set to 50% for each battery during the calendar ageing. The accelerated calendar ageing test lasted for 360 days, and a performance test was carried out every 30 days to measure the battery capacity at present. During the performance test, the ambient temperature is set to 25 °C and the sampling time is 1 s.

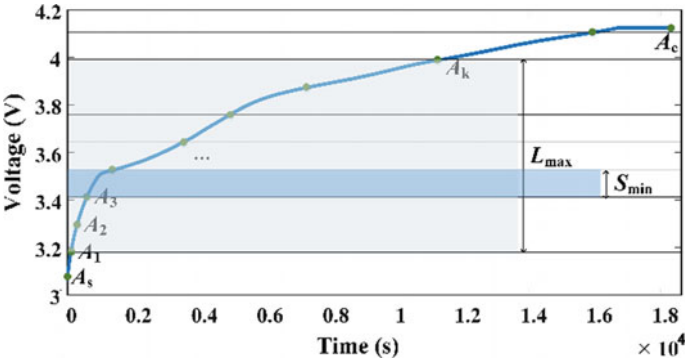

Fig. 4.13 Optimal signal voltage selection with grid search, reprinted from [53], with permission from Elsevier

Table 4.3 Accelerated calendar ageing condition

Temperature (°C)	35	40	45
SoC = 50%	Cell 1	Cell 2	Cell 3

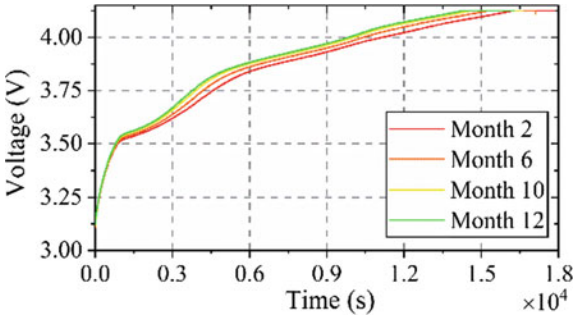

Fig. 4.14 The voltage curves of Cell 1 during the calendar ageing, reprinted from [53], with permission from Elsevier

The voltage profile of Cell 1 during the degradation test is shown in Fig. 4.14. The voltage measurement from Cell 2 and 3 shows a similar result. The voltage profiles gradually shift to the vertical axis because less energy can be stored in an aged cell.

Once grid search is used, one optimal voltage range can be found. We set the search step $S_{\min}$ to 0.1 V. Then, we find the optimal voltage ranges of the three NMC cells as shown in Fig. 4.15. According to these selected voltage ranges, the estimation results of the three cells are obtained as illustrated in Fig. 4.16.

The effectiveness of battery capacity estimation with one optimal voltage profile is proved by the results in Fig. 4.17. The estimation results are very close to the reference during the degradation procedure. The MSE is 2.5227×10^{-5} for Cell 1, 2.3441×10^{-5} for Cell 2 and 1.5151×10^{-5} for Cell 3. The optimal voltage range of Cell 1 in the first month of the calendar ageing is taken as an example in Fig. 4.17. The length of the voltage range is 12,669 s.

Notably, grid search can only provide one specific optimal solution for the SOH estimation. Although the EV users definitely charge their battery pack [54], it does not mean that the variation of the voltage profile will cover the specific optimal voltage range each time. Moreover, the width of the voltage ranges should also be considered in reality. A shorter voltage range means a higher efficiency. The two requirements conflict with each other in most situations. For instance, collecting measurement of the voltage profile as much as possible enhances the estimation accuracy, while deteriorating the overall efficiency. On the contrary, using limited data is easy for the

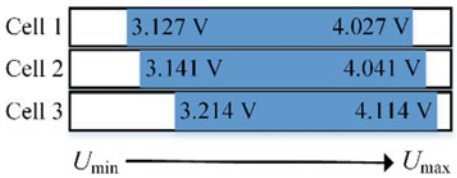

Fig. 4.15 Optimal voltage ranges of the three NMC cells, reprinted from [53], with permission from Elsevier

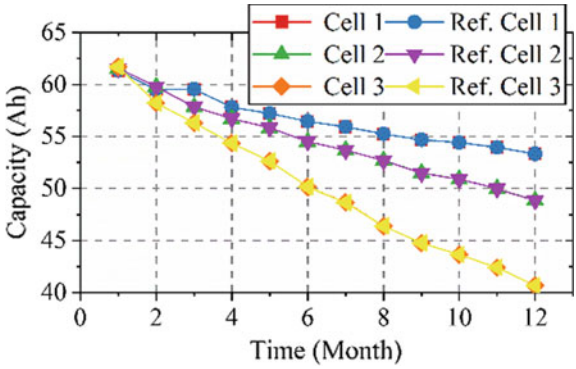

Fig. 4.16 Estimation results of the three cells, reprinted from [53], with permission from Elsevier

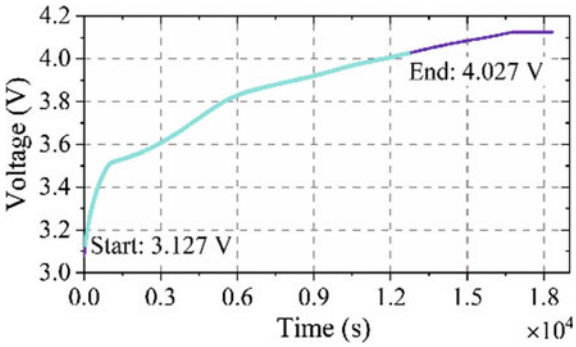

Fig. 4.17 Optimal voltage range of Cell 1, reprinted from [53], with permission from Elsevier

measurement, but the estimation accuracy may not be guaranteed. Hence, we need to solve a bi-objective optimization problem here for the best trade-off solutions. In order to conveniently obtain the voltage range in real applications, NSGA-II is used to choose two optimal voltage ranges considering both the length of the voltage profile and the accuracy of the capacity estimation. In addition, a series of non-dominated solutions from NSGA-II provide more freedom for BMS to estimate the battery SOH at various ageing stages.

The procedure of NSGA-II finding the two optimal voltage intervals are illustrated in Fig. 4.18. The voltage curve during the battery degradation is collected to form the original dataset. Afterwards, the initial populations are created by NSGA-II, which can reach multiple optimal solutions within one iteration. After evaluating the fitness of each individual, a fast non-dominated sorting algorithm is applied to assign the non-dominated level of each candidate solution. Additionally, the crowding distance is given to each individual. The new populations are selected from the best non-dominated set, and the solutions in the same non-dominated level are evaluated by the crowded comparison operator. Selection, crossover, and mutation are used to

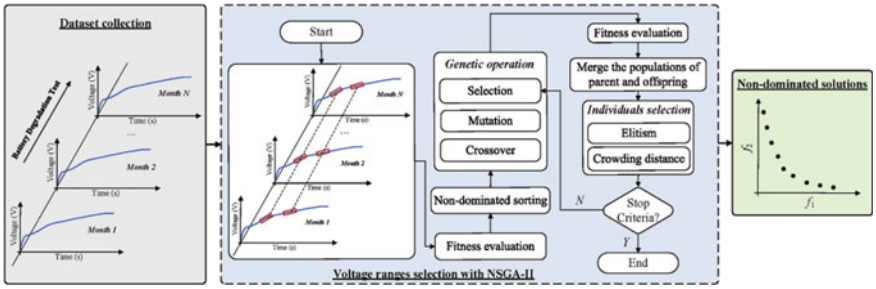

Fig. 4.18 Procedure of two voltage ranges selection with NSGA-II, reprinted from [53], with permission from Elsevier

generate the offspring from the current populations. Once the stop criteria are met, the partial charging voltages are found by NSGA-II.

In NSGA-II, each individual is encoded into a chromosome-like structure as shown in Fig. 4.19. The chromosome-like structure in Fig. 4.19a consists of four numbers U_{A1}, U_{A2}, U_{B1}, U_{B2}. From Fig. 4.19b, we know that U_{A1} and U_{A2} are the start and end points of the first voltage range, U_{B1} and U_{B2} are the corresponding points for the second voltage range.

The cost function of NSGA-II is well designed to evaluate the fitness of each individual. As the main purpose of the proposed method is the estimation accuracy, MSE of the estimation is used as one of the cost functions in Eq. (4.36).

$$f_1 = \frac{1}{n}\sum_{i=1}^{n}\left(Q_i - \hat{Q}_i\right)^2 \tag{4.36}$$

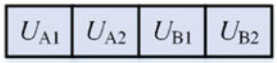

(a) The chromosome-like structure

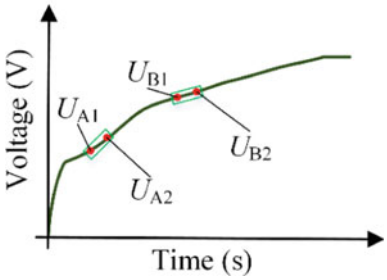

(b) The voltage ranges

Fig. 4.19 Individual representation, reprinted from [53], with permission from Elsevier

where Q_i is the reference capacity and $\hat{Q}_i$ is the estimated capacity, and n is number of the reference values during the degradation test. Thus, a smaller f_1 means a more accurate estimation. For the two voltage ranges condition, the battery capacity can be calculated as,

$$\widehat{Q}_i = \frac{\sum_{k=A_1}^{A_2} \eta \cdot I(k) \cdot T_s + \sum_{k=B_1}^{B_2} \eta \cdot I(k) \cdot T_s}{[\mathrm{SoC}(A_2) - \mathrm{SoC}(A_1)] + [\mathrm{SoC}(B_2) - \mathrm{SoC}(B_1)]} \tag{4.37}$$

The above equations mean that the SOC variations and the current integration of the two voltage ranges are accumulated, respectively. From the practical point of view, the length of the voltage ranges ($U_{A_1} \sim U_{A_2}$ and $U_{B_1} \sim U_{B_2}$) should be as small as possible for the purpose of conveniently obtaining the measurement from real applications. Thus, the cost function f_2 is defined as,

$$f_2 = \frac{1}{n} \sum_{i=1}^{n} \left(L_{U_{A1}-U_{A2}} + L_{U_{B1}-U_{B2}} \right) \tag{4.38}$$

where $L_{U_{A1}-U_{A2}}$ is the length between U_{A1} and U_{A2}, and $L_{U_{B1}-U_{B2}}$ is the length between U_{B1} and U_{B2}. Because the length of the voltage charging profile changes from week to week, the average length is chosen to calculate the f_2 during the battery degradation. Thus, a smaller f_2 is preferred because less voltage measurement is needed in this condition.

In practical, the two voltage ranges are time series measurement, and U_{A2} may not less than U_{A1} in a single range. Therefore, the constraints of the proposed method can be expressed as,

$$U_{A2} > U_{A1} \quad \text{and} \quad U_{B2} > U_{B1} \tag{4.39}$$

In this data science-based method, a special designed operator is applied to discard those illegal solutions in the selection operation. That is, a new solution will be selected only if the condition [Eq. (4.39)] is fulfilled. Otherwise, this solution has to be discarded, and the variation will be repeated until the new created solution is suitable for the constraints.

The value of f_1 and f_2 are in different ranges, and they are normalized between 0 and 1 for a better illustration, as shown in Fig. 4.20. All the solutions in the Pareto front of Fig. 4.20 are the optimal choice from a specific point of view. In Fig. 4.20, 50 non-dominated solutions form the Pareto front. Hence, various candidate solutions can be used to estimate battery SoH at different charging stages.

In this subsection, we only choose to show three typical solutions of Cell 1 in Fig. 4.21. The MSEs of each typical solution are listed in Table 4.4. The three typical solutions include two long voltage ranges (Solution A) and two short voltage ranges (Solution B and C). In Fig. 4.21, the two voltage ranges have some overlap for Solution A, while the two voltage ranges are separated and much shorter for

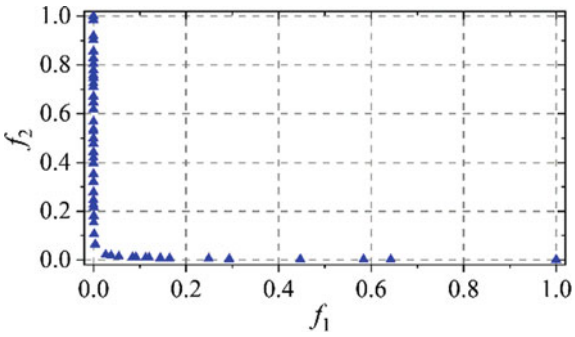

Fig. 4.20 Non-dominated solutions from NSGA-II, reprinted from [53], with permission from Elsevier

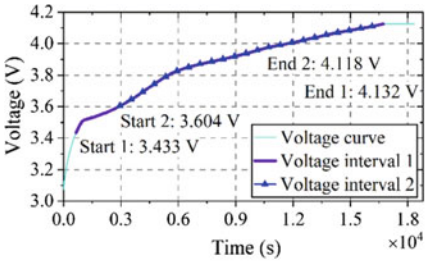

(a) Solution A

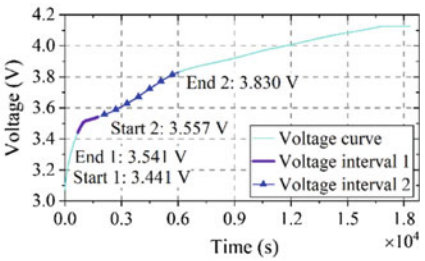

(b) Solution B

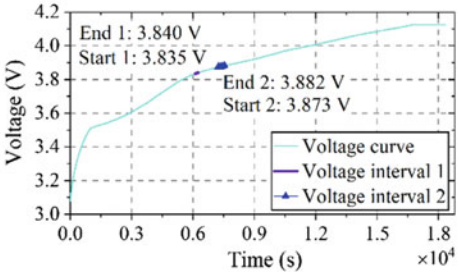

(c) Solution C

Fig. 4.21 Three typical solutions of Cell 1, reprinted from [53], with permission from Elsevier

Table 4.4 MSEs of the three typical solutions

Solution	A	B	C
MSE	1.75×10^{-5}	6.97×10^{-4}	8.96×10^{-2}

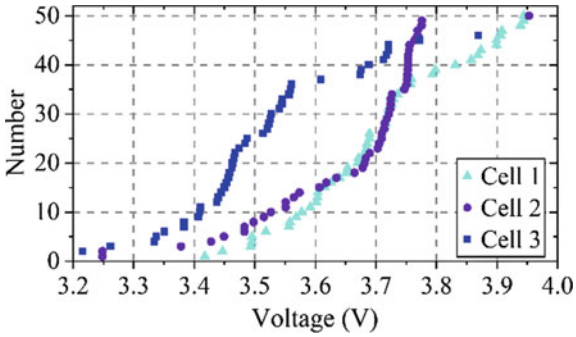

Fig. 4.22 Starting points of the non-dominated solutions of each cell, reprinted from [53], with permission from Elsevier

Solutions B and C. Compared with single voltage range, two voltage ranges provide more flexibility to estimate the SoH with partial charging profile.

The non-dominated solutions in different cells have some similarities as shown in Fig. 4.22. We can find that the starting points of the three cells are quite close to each other. For the starting points of one cell, there are always a starting point nearby for the other two cells. This indicts the generalization of the solutions from Cell 1 to Cells 2 and 3.

In order to further verify the generalization of the proposed method, the optimal voltage ranges from Cell 1 are directly applied to estimate the capacity of Cells 2 and 3. The three typical solutions of Cell 1 in Fig. 4.21 are validated by Cells 2 and 3. We can see the three typical solutions from Cell 1 also receive accuracy capacity estimation of Cells 2 and 3 in Fig. 4.23, which proves the generalization of the proposed method.

In the previous validation of this section, the SoC in the calculation comes from the Coulomb counting method with a known initial value. The reason is that the NMC batteries are always fully charged or discharged in our life time test. However, an initial SoC is hardly to be known in the real applications. The most popular estimation method in this area is the model-based SoC estimation methods, which can only provide less than $\pm 2\%$ error band. A $\pm 5\%$ error band is added to the SoC for verifying the accuracy of the proposed method. The denominator of Eq. (4.35) is the subtraction of $\mathrm{SoC}(A_1)$ and $\mathrm{SoC}(A_2)$, and the maximum and minimum of $\Delta\mathrm{SoC}$ is expressed as:

$$\begin{cases} \Delta\mathrm{SoC}_{\min} = \mathrm{SoC}_{-5\%}(A_2) - \mathrm{SoC}_{+5\%}(A_1) \\ \Delta\mathrm{SoC}_{\max} = \mathrm{SoC}_{+5\%}(A_2) - \mathrm{SoC}_{-5\%}(A_1) \end{cases} \tag{4.40}$$

where $\mathrm{SoC}_{-5\%}(\cdot)$ is the SOC including -5% error, and $\mathrm{SoC}_{+5\%}(\cdot)$ is the SoC with $+5\%$ error.

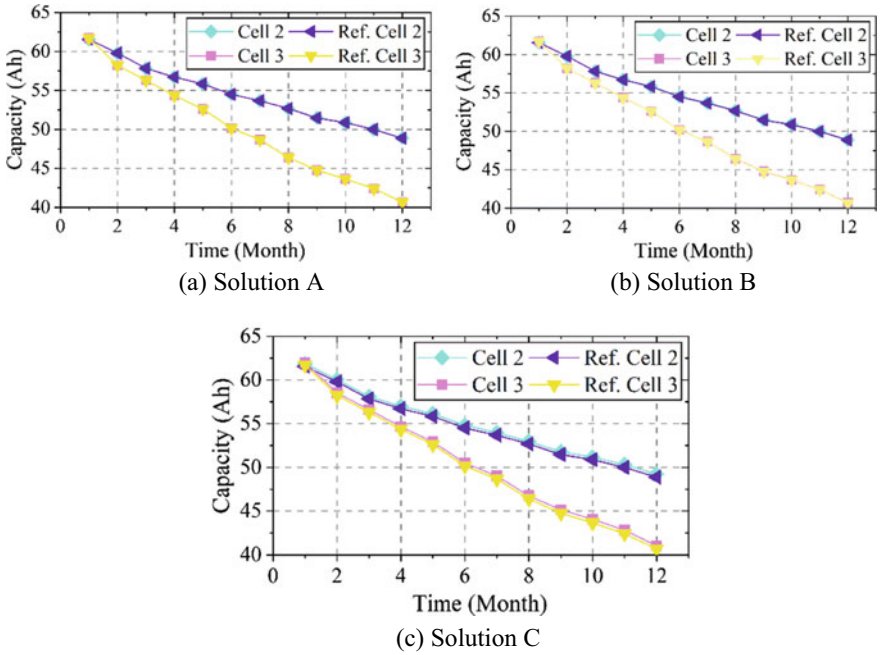

Fig. 4.23 Validation of three typical solutions from Cell 1 on Cells 2 and 3, reprinted from [53], with permission from Elsevier

In order to verify the effect of SoC estimation error on the performance of the proposed method, the voltage range [3.127 V, 4.027 V] is applied to estimate the capacity of Cell 1. The estimation results in Fig. 4.24 give the error band of the proposed method. Although ±5% SoC estimation error is added, the maximum absolute error of the estimation results is 3.2539 Ah, which is 5.16% of the battery

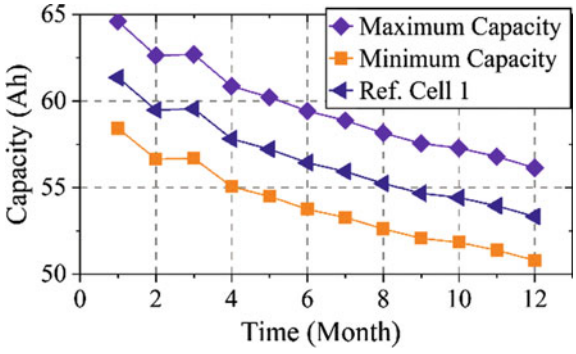

Fig. 4.24 Effect of SOC estimation error on the proposed method, reprinted from [53], with permission from Elsevier

nominal capacity as shown in Fig. 4.24. Thus, we can ensure the capacity estimation error of the proposed method is still in a small limited range when large SoC estimation error exists.

4.2.4 *Joint State Estimation*

Currently, there are a great deal of works focus on battery single state estimation in the literature, whereas the researches of joint estimation (co-estimations of at least two states) of battery multi-states are limited. It should be known that during operations, battery states would be coupled and interact with each other. Estimating just one state without considering others would cause only relatively satisfactory results under a certain constraint. In this context, for better operation management of batteries, the joint state estimation of battery considering the effects of different internal states is urgently required.

4.2.4.1 Definition of Battery Joint State Estimation

Figure 4.25 illustrates the relations of several strong-coupled battery critical states. Specifically, due to the fast-variations of battery electric dynamics, battery SoC and SoP would rapidly change with a short-term timescale. According to the battery physics structure and heat transfer nature, battery macroscopic states such as state

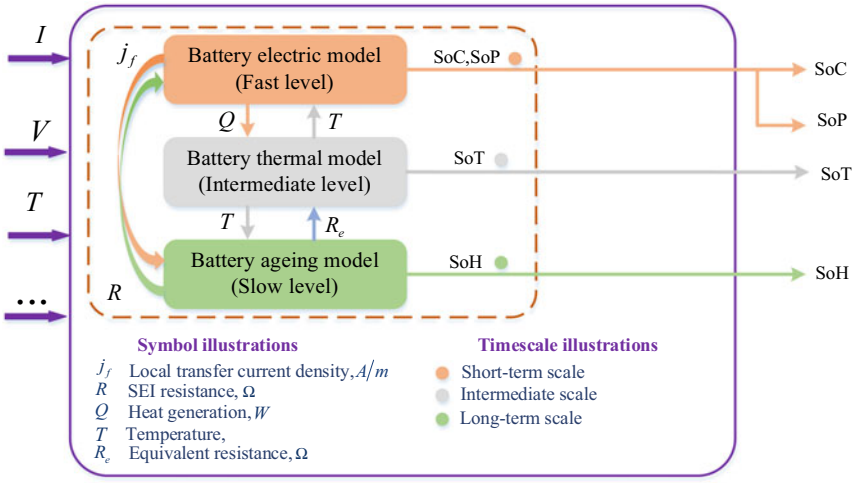

Fig. 4.25 Several battery key internal states with different timescale (here I, V, and T_f represent battery terminal current, voltage and surface temperature, respectively), reprinted from [32], with permission from Elsevier

of temperature (SoT) would change with an intermediate timescale [55]. For battery SoH, as it is manifested by several slow-variation factors such as internal impedance or resistance increase and capacity degradation, this state would change slowly with a long-term timescale during battery operations.

To date, just a few existing data science researches focus on double-states co-estimations of battery. Among these researches, the joint estimation of both battery SoC and SoH plays a dominant position. This is primarily caused by the fact that updating battery SoH information (capacity or resistance) periodically is crucial for enhancing the estimation performance of battery SoC. Based upon the equivalent circuit models or electrochemical models, various data science observers including the Kalman filter (KF) [46], adaptive filter [56], and their variants, such as the extended KF (EKF) [57], dual-fractional-order extended KF (DEKF) [46], have been designed to effectively co-estimating battery SoC and SoH simultaneously. Besides, apart from joint-estimating battery SoC and SoH, limited data science research has been also done to estimate other battery double-states, such as the co-estimations of battery SoC and SoP [58], SoC and SoT [59]. Furthermore, compared with only one battery state estimation, larger computational burden is generally required for joint state estimation applications. In this context, to widen battery joint state estimations, state-of-the-art data science solutions such as the fractional order calculus [46] and multi-timescale estimators [60] that could enhance co-estimation accuracy and provide a satisfactory computational effort are becoming a promising research direction.

4.2.4.2 Case Study: Battery SoC and SoH Co-estimation with Enhanced Electrochemical Model

In this subsection, a data science case study through developing an enhanced electrochemical model to achieve the high-fidelity co-estimation of SoC and SoH is presented [61]. To be specific, the full-order battery Pseudo-two-dimensional (P2D) model is first simplified based on the Padé approximation while ensuring precision and observability. Next, the feasibility and performance of SoC estimator are revealed by accessing unmeasurable physical variables, such as the surface and bulk solid-phase concentration. To well reflect battery degradation, three key ageing factors including the loss of lithium ions, loss of active volume fraction, and resistance increment are simultaneously identified, leading to an appreciable precision improvement of SoC estimation online particular for aged cells. Finally, extensive verification experiments are carried out over the cell's lifespan to demonstrate the performance of this SoC/SoH co-estimation scheme.

Figure 4.26 illustrates the schematic of the typical battery P2D model, where the Li-ions are assumed to diffuse with the directions of x and r. Here, the particle would be uniformly distributed with a radius of R_s. In general, four governing equations including the conservation of Li^+ and charge in both solid as well as electrolyte phases are adopted to formulate a battery electrochemical model. The diffusion of Li^+ within a single particle is generally captured by the Fick's law as [62]:

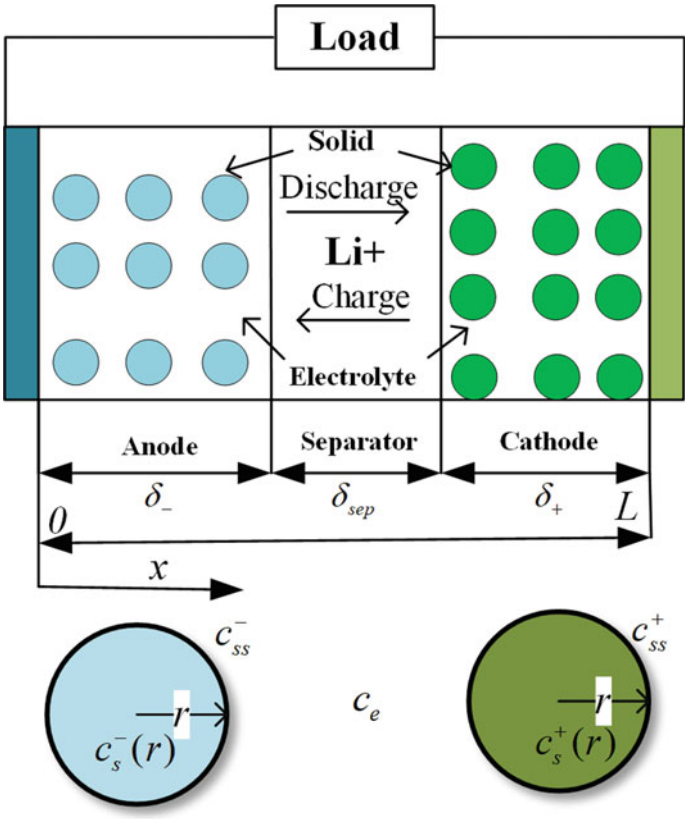

Fig. 4.26 Schematic of the typical battery P2D model, reprinted from [61], with permission from IEEE

$$\frac{\partial c_s}{\partial t} = \frac{D_s}{r^2}\frac{\partial}{\partial r}\left(r^2\frac{\partial c_s}{\partial r}\right) \tag{4.41}$$

where D_s is a coefficient to reflect solid diffusion, and c_s represents the concentration of Li^+ within solid phase. c_{ss} means the concentration of particle surface at $r = R_s$. $c_{ss}(t) = c_s(R_s, t)$. The bulk concentration $\overline{c}_s^{\pm}$ in the anode/cathode can be obtained by:

$$\frac{\partial \overline{c}_s}{\partial t} = \frac{I}{FA_{\text{cell}}\delta\varepsilon_s} \tag{4.42}$$

where I reflects input current. F and A_{cell} are Faraday constant and electrode surface area, respectively. δ stands for electrode thickness, while ε_s means the active materials' volume fraction. The lithium concentration c_e of electrolyte can be expressed

by:

$$\varepsilon_e \frac{\partial c_e}{\partial t} = D_e^{\text{eff}} \frac{\partial^2 c_e}{\partial x^2} + \frac{a_s\left(1 - t_+^0\right)}{F} j \tag{4.43}$$

where D_e^{eff} reflects the diffusion coefficient of effective electrolyte. ε_e means the electrolyte's volume fraction, while t_+^0 stands for the transference number of Li^+. j is the lithium flux density. Conservation of charge in the solid phase generates a governing equation of potential in the solid phase ϕ_s as:

$$\sigma^{\text{eff}} \frac{\partial^2 \phi_s}{\partial x^2} - a_s j = 0 \tag{4.44}$$

where σ^{eff} and a_s are specific interfacial surface area and effective electrode conductivity, respectively. Conservation of charge in the electrolyte phase generates the equation to reflect the potential of electrolyte phase ϕ_e as:

$$k^{\text{eff}} \frac{\partial^2 \phi_e}{\partial x^2} + k_d^{\text{eff}} \frac{\partial^2 \ln c_e}{\partial x^2} + a_s j = 0 \tag{4.45}$$

where k^{eff} and k_d^{eff} are the effective ionic and diffusion conductivities, respectively. Here, the Butler–Volmer equation is adopted to control the electrochemical kinetics as:

$$j = i_0 \left(\exp\left(\frac{\alpha_a F}{RT} \eta \right) - \exp\left(-\frac{\alpha_c F}{RT} \eta \right) \right) \tag{4.46}$$

where i_0 is the exchange current density. α_a and α_c are coefficients to reflect anode and cathode charge transfer, respectively. R and T are universal gas constant and temperature, respectively. Overpotential η is the extra force needed to overcome surface reaction by:

$$\begin{aligned} \eta_p(t) &= \phi_s(L, t) - \phi_e(L, t) - U_p(c_{ss}^+) \\ \eta_n(t) &= \phi_s(0, t) - \phi_e(0, t) - U_n(c_{ss}^-) \end{aligned} \tag{4.47}$$

where U_p is cathode open-circuit potential, and U_n is anode open-circuit potential. Here the cell terminal voltage could be described by:

$$V(t) = \phi_s(L, t) - \phi_s(0, t) - R_f I \tag{4.48}$$

where R_f stands for the summation of solid electrolyte interface (SEI) resistance and ohmic resistance [63].

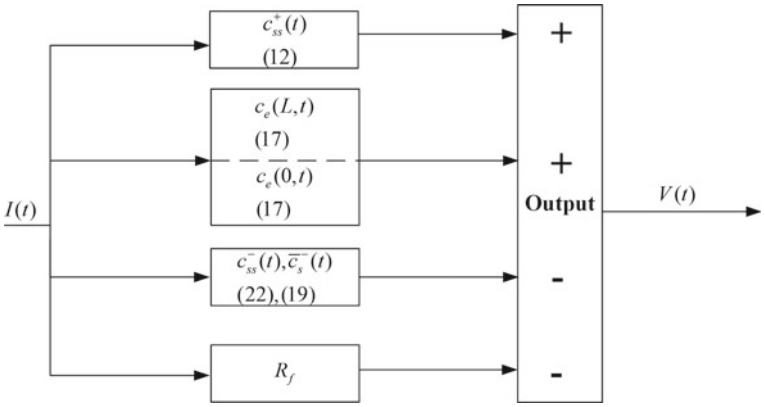

Fig. 4.27 Diagram of simplified battery electrochemical model, reprinted from [61], with permission from IEEE

The final expression of terminal voltage could be obtained by substituting Eq. (4.47) into Eq. (4.48):

$$\begin{aligned} V(t) = &(U_p(c_{\text{ss}}^{+}) + \eta_p(t) + \phi_e(L,t)) \\ &- (U_n(c_{\text{ss}}^{-}) + \eta_n(t) + \phi_e(0,t)) - R_f I(t) \end{aligned} \tag{4.49}$$

Based upon the above discussion, Fig. 4.27 illustrates the block diagram of battery reduced-order electrochemical model as:

To simplify electrochemical model, Eq. (4.41) could be further modified after taking Laplace transform as:

$$\frac{C_{\text{ss}}(R_s, s)}{J(s)} = \frac{R_s}{a_s F D_s} \frac{\tanh\left(\sqrt{\frac{s}{D_s}} R_s\right)}{\tanh\left(\sqrt{\frac{s}{D_s}} R_s\right) - \sqrt{\frac{s}{D_s}} R_s} \tag{4.50}$$

where a_s, F, and D_s are the specific interfacial area, Faraday constant, and diffusion coefficient of solid-phase Li^+, respectively.

Then a third-order Padé approximation [64] is adopted to convert Eq. (4.50) into a polynomial transfer function as:

$$\frac{C_{\text{ss}}(s)}{J(s)} = \pm \frac{\frac{3}{R_S} + \frac{4R_S}{11D_S} s + \frac{R_S^3}{165D_S^2} s^2}{a_s F (s + \frac{3R_S^2}{55D_S} s^2 + \frac{R_S^4}{3465D_S^2} s^3)} \tag{4.51}$$

Equation (4.51) can be further transformed into a state-space equation with the controller canonical form as:

$$\begin{aligned}
\dot{x}_i &= A_i x_i + B_i u \\
A_i &= \begin{bmatrix} 0 & 1 & 0 \\ 0 & 0 & 1 \\ 0 & -\frac{3465D_s^2}{R_s^4} & -\frac{2079}{11R_s^2} \end{bmatrix}, \quad B_i = \begin{bmatrix} 0 \\ 0 \\ \pm\frac{3465D_s^2}{a_s F R_s^4} \end{bmatrix} \\
c_{ss} &= \begin{bmatrix} \frac{3}{R_s} & \frac{4R_s}{11D_s} & \frac{R_s^3}{165D_s^2} \end{bmatrix} x_i \\
\overline{c}_s &= \begin{bmatrix} \frac{3}{R_s} & \frac{9R_s}{55D_s} & \frac{R_s^3}{1155D_s^2} \end{bmatrix} x_i
\end{aligned} \tag{4.52}$$

where $i = \{p, n\}$, $x_i = [\, x_1 \; x_2 \; x_3 \,]^T$, u is the input current. Here, x_1, x_2, and x_3 are utilized to describe the surface c_{ss} and bulk $\overline{c}_s$ lithium concentration in the electrodes without physical meanings.

According to the Taylor expansion, the Butler–Volmer equation could be linearized by:

$$\eta(s) = \frac{RT}{F i_0 (\alpha_a + \alpha_c)} J(s) \tag{4.53}$$

where α_a is the symmetric anodic reaction charge transfer coefficient, and α_c the symmetric cathodic one. i_0 stands for the exchange current density that is correlated with ion concentrations by: $i_0 = k(C_e)^{\alpha_a}(C_{s,\max} - C_{ss})^{\alpha_a}(C_{s,\max} - C_{ss})^{\alpha_c}$.

Here, the intercalation current density of electrode is proportional to battery current as:

$$J(s) = \frac{I}{A_{\mathrm{cell}} F \delta a_s} \tag{4.54}$$

After adopting the analytical solution with first-order Padé approximation [45], electrolyte potential difference from Eq. (4.45) could be derived by:

$$\frac{C_e(L, s)}{J_p(s)} = \frac{1}{b_{1,p}s + b_{2,p}} \tag{4.55}$$

$$\frac{C_e(0, s)}{J_n(s)} = \frac{1}{b_{1,n}s + b_{2,n}} \tag{4.56}$$

Here, $b_{1,p}$, $b_{2,p}$, $b_{1,n}$, and $b_{2,n}$ are all constant parameters. Equations (4.55) and (4.56) could be expressed by state-space form as:

$$\begin{aligned}
\dot{x}_e &= A x_e + B u \\
A &= \begin{bmatrix} -\frac{b_{2,p}}{b_{1,p}} & 0 \\ 0 & -\frac{b_{2,n}}{b_{1,n}} \end{bmatrix}, \quad B = \begin{bmatrix} \frac{1}{b_{1,p}} \\ \frac{1}{b_{2,n}} \end{bmatrix}
\end{aligned}$$

$$\begin{bmatrix} c_{e,L} \\ c_{e,0} \end{bmatrix} = \begin{bmatrix} 1 & 1 \end{bmatrix} x_e \tag{4.57}$$

where u stands for battery current, x_e is a vector with one-dimension to represent the electrolyte concentration at $x = 0/L$.

Next, the derived data science observer for the co-estimation of battery SoC and SoH is proposed in detail. Specifically, after the above simplification of P2D model, battery terminal voltage from Eq. (4.49) can be described by:

$$\begin{aligned} V(t) = {} & U_p(c_{ss}^+) - U_n(c_{ss}^-) \\ & + \eta_p(i_{0,p}(c_{ss}^+, c_{e,p})) - \eta_n(i_{0,p}(c_{ss}^-, c_{e,n})) \\ & + \phi_e(c_{e,L}) - \phi_e(c_{e,0}) - R_f I \end{aligned} \tag{4.58}$$

To decrease the condition number for battery SoC estimator, one effective data science solution through estimating the lithium concentration of negative electrode with the open-loop simulations of positive electrode as well as liquid phase is adopted. In this context, the positive electrode and liquid potentials subtracted from battery terminal voltage could be utilized as the feedback of anode observer. According to Eq. (4.52), the model formulation of SoC estimation part is:

$$\begin{aligned} & \dot{x}_n = f(x_n, u) = Ax_n + Bu \\ & A = \begin{bmatrix} 0 & 1 & 0 \\ 0 & 0 & 1 \\ 0 & -\frac{3465 D_{s,n}^2}{R_{s,n}^4} & -\frac{2079}{11 R_{s,n}^2} \end{bmatrix}, \quad B = \begin{bmatrix} 0 \\ 0 \\ -\frac{3465 D_{s,n}^2}{a_{s,n} F R_{s,n}^4} \end{bmatrix} \\ & g(x_n, u) = \phi_s^- = U_n + \eta_n + R_f I \end{aligned} \tag{4.59}$$

where $x_n = [\, x_1 \; x_2 \; x_3 \,]^T$, u represents the input current.

For battery SoH estimation part, the recyclable lithium loss caused by the side reaction of anode would lead to the shift of $\theta_{100\%,n}$ (upper voltage limits) and $\theta_{0\%,n}$ (lower voltage limits), respectively. In this context, lithium ions loss could be determined through estimating the concentration of normalized anode bulk with the fully charging or discharging state. Here, the analogical open-loop framework would be adopted to facilitate anode observer. With regard to active material loss and internal resistance increase, the estimation of these two ageing factors becomes the monitoring of $\varepsilon_{s,\text{neg}}$ and R_f within the model. Therefore, $\varepsilon_{s,\text{neg}}$ and R_f are treated as another states within anode observer in the designed joint estimation framework. In the light of this, equations to describe state dynamics of anode are expressed as:

$$\dot{x}_\theta = f(x_\theta, u) = Ax_\theta + Bu$$

$$A = \begin{bmatrix} 0\,0\,0 \\ 0\,0\,0 \\ 0\,0\,0 \end{bmatrix}, \quad B = \begin{bmatrix} \frac{-1}{FA_{\text{cell}}\delta_- \varepsilon_{s,n}} \\ 0 \\ 0 \end{bmatrix}$$
$$g(x_\theta, u) = \phi_s^- = U_n + \eta_n + R_f I \tag{4.60}$$

where $x_\theta = [\,\theta_1\ \theta_2\ \theta_3\,]^T$, u represents battery current. Here, θ_1 would determine bulk concentration of graphite electrode. The time derivatives of anode's bulk concentration have been shown in Eq. (4.60). θ_2 and θ_3 represent the active material volume of anode $\varepsilon_{s,n}$ and interior resistance R_f, respectively. The time derivatives of $\varepsilon_{s,n}$ and R_f are set to zero. Afterwards, the observability of derived SoC and SoH co-estimator could be described by the *Lie derivatives*. Here, the simplified battery model equations is reformulated by:

$$\begin{aligned} \dot{x}_{n/\theta} &= f(x_{n/\theta}, u) + w \\ y &= g(x_{n/\theta}, u) + v \end{aligned} \tag{4.61}$$

where x and u represent state and input, respectively. w is system noise while v is measurement noise. The $N-1$ order *Lie derivatives* of g is expressed by:

$$\begin{aligned} &L_f^0(g) = g(x_{n/\theta}, u) \\ &\vdots \\ &L_f^{N-1}(g) = g^{N-1}(x_{n/\theta}, u, \dot{u}, \ldots, u^{(N-1)}) \end{aligned} \tag{4.62}$$

According to the Jacobian of *Lie derivatives* set [23], the observability matrix could by expressed as:

$$\Theta = \begin{bmatrix} \frac{\partial L_f^0(g)}{\partial x_{n/\theta,1}} & \cdots & \frac{\partial L_f^0(g)}{\partial x_{n/\theta,N}} \\ \vdots & \ddots & \vdots \\ \frac{\partial L_f^{N-1}(g)}{\partial x_{n/\theta,1}} & \cdots & \frac{\partial L_f^{N-1}(g)}{\partial x_{n/\theta,N}} \end{bmatrix} \tag{4.63}$$

where $x_{n/\theta,N}$ represents the Nth element of $x_{n/\theta}$.

To simultaneously estimate both battery states and parameters of the simplified electrochemical model, a dual extended Kalman filter (DEKF) is adopted. To be specific, SoC estimation under a fast timescale is realized by one filter based on the known ageing parameters, while SoH estimation under slow timescale is realized by using another filter to identify related ageing parameters online. Figure 4.28 details the whole scheme for battery SoC and SoH co-estimation, where the corresponding parameters are described in Table 4.5. Here, Q and R are the covariance matrixes of process and sensor noises. All four ageing parameters $\theta_{100\%,n}$, $\theta_{0\%,n}$, $\varepsilon_{s,n}$ and R_f in

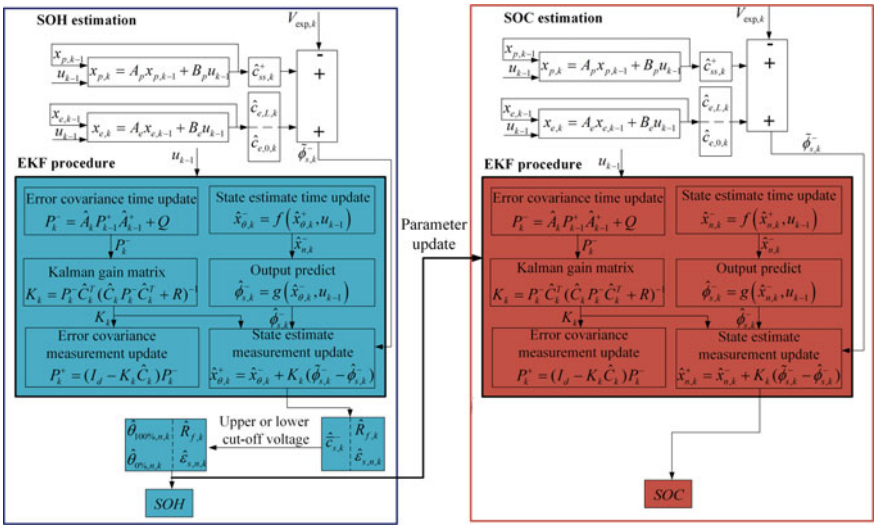

Fig. 4.28 Schematic of joint estimation of battery SoC and SoH, reprinted from [61], with permission from IEEE

Table 4.5 EKF parameters and procedure, reprinted from [61], with permission from IEEE

	EKF for SoC estimation	EKF for SoH estimation
$\widehat{A}_k$	$\frac{\partial f(x_{n,k},u_k)}{\partial x_{n,k}}\Big\vert x_{n,k} = \hat{x}^+_{n,k}$	$\frac{\partial f(x_{\theta,k},u_k)}{\partial x_{\theta,k}}\Big\vert x_{\theta,k} = \hat{x}^+_{\theta,k}$
$\widehat{C}_k$	$\frac{\partial g(x_{n,k},u_k)}{\partial x_{n,k}}\Big\vert x_{n,k} = \hat{x}^-_{n,k}$	$\frac{\partial g(x_{\theta,k},u_k)}{\partial x_{\theta,k}}\Big\vert x_{\theta,k} = \hat{x}^-_{\theta,k}$
Q	$10^{-9} \times \text{diag}(4, 2, 27)$	$10^{-16} \times \text{diag}(4, 2800, 9000)$
R	4×10^{-3}	6×10^{-2}

Initialization for $k = 0$

$\hat{x}^+_{n/\theta,0} = E\left[x_{n/\theta,0}\right]$

$P^+_0 = E[\left(x_{n/\theta,0} - \hat{x}^+_{n/\theta,0}\right)\left(x_{n/\theta,0} - \hat{x}^+_{n/\theta,0}\right)^T]$

Iteration for $k = 1, 2, \ldots$

State-prediction time update: $\hat{x}^-_{n/\theta,k} = f\left(\hat{x}^+_{n/\theta,k}, u_{k-1}\right)$

Error-covariance time update: $P^-_k = \widehat{A}_k P^+_{k-1} \widehat{A}^+_{k-1} + Q$

Output estimate: $\hat{y}^-_k = g(\hat{x}^-_{n/\theta,k}, u_{k-1})$

Estimator gain matrix: $K_k = P^-_k \widehat{C}^T_k (\widehat{C}_k P^-_k \widehat{C}^T_k + R)^{-1}$

State-estimate measurement update: $\hat{x}^+_{n/\theta,k} = \hat{x}^-_{n/\theta,k} + K_k(y_k - \hat{y}^-_k)$

Error-covariance measurement update: $P^+_k = (I_d - K_k \widehat{C}_k) P^-_k$

battery SoC estimation block would be periodically updated from related predictions of SoH estimation block, further benefitting the accuracy of SoC estimator over time.

Next, the effectiveness of the proposed co-estimation scheme is verified against the experimental results of battery cycling tests. A series of characterization tests, including a dynamic stress test (DST) cycle and an Urban Dynamometer Driving Schedule (UDDS) cycle, are performed on the NCM/graphite18650 batteries every two weeks. The cycling test schedule is depicted in Fig. 4.29.

Before implementing the SoC/SoH co-estimation algorithm, it is necessary to validate the accuracy of electrochemical model. Figure 4.30 illustrates the voltage responses of the developed model with both static load (1C CCCV charging, CC discharging) and dynamic load (UDDS, DST cycles with 3C maximum current). The predicted voltage shows good agreement with the measured voltage. The simplified

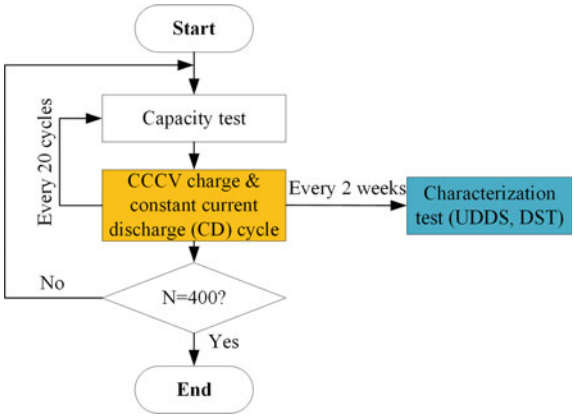

Fig. 4.29 Cyclic test process to generate battery experimental data, reprinted from [61], with permission from IEEE

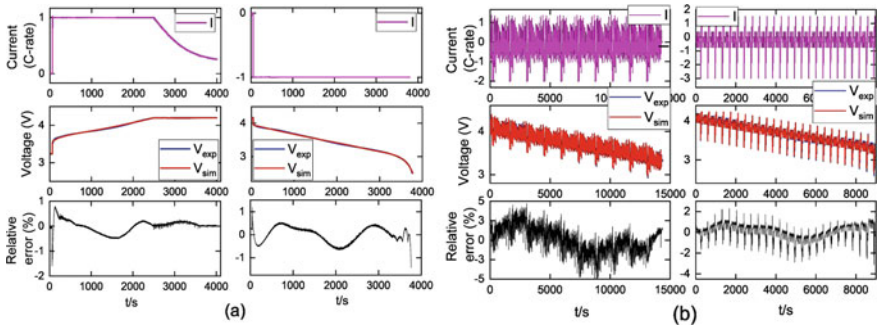

Fig. 4.30 Experimental validation of enhanced electrochemical model: **a** 1C CCCV charging and CC discharging, **b** UDDS cycles with 2C maximum current, and DST cycles with 3C maximum current, reprinted from [61], with permission from IEEE

model achieves a voltage RMSE of {10.52, 11.85, 23.25, 21.34 mV} for these cases of CCCV charge, CC discharge, UDDS cycles, and DST cycles, respectively. The results indicate that the model parameters are initialized properly.

To verify the effectiveness of proposed data science method for SoH estimation, a single CC discharging and CCCV charging cycle is adopted. Here, the state and parameter estimates are randomly initialized as: $\hat{\theta}_n(0) = 0.7\theta_n^*(0)$, $\hat{\varepsilon}_{s,n}(0) = 0.5\varepsilon_s^*$, and $\widehat{R}_f(0) = 2R_f^*$. After inputting the measured voltage and current, the evolutions of both state and parameter estimates are illustrated in Fig. 4.31. It can be seen that although there exists large initial errors, $\hat{\theta}_n$, $\hat{\varepsilon}_{s,n}$, and $\widehat{R}_f$ could converge to their nominal values within 3000 s of discharging process.

Figure 4.32a–d illustrates the capacity estimation results of four cells with different ageing levels. For fresh cell in Fig. 4.32a, the capacity estimates with CD-CCCV, UDDS, and DST tests all converge to the measured capacity gradually even these estimates are initialized with incorrect values, indicating the effectiveness of the observer. Similar estimation performance can be achieved at ageing levels 2, 3, and 4, as shown in Fig. 4.32b–d. Figure 4.33a and b shows the capacity estimation perfor-

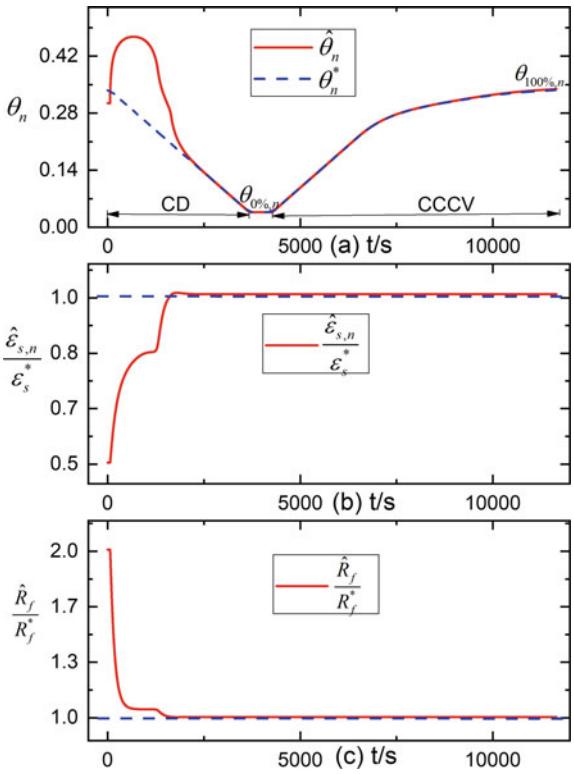

Fig. 4.31 Evolution of estimated parameters with CC discharging-CCCV charging cycle: **a** $\theta_{100\%,n}$, $\theta_{0\%,n}$, **b** $\varepsilon_{s,n}$, and **c** R_f, reprinted from [61], with permission from IEEE

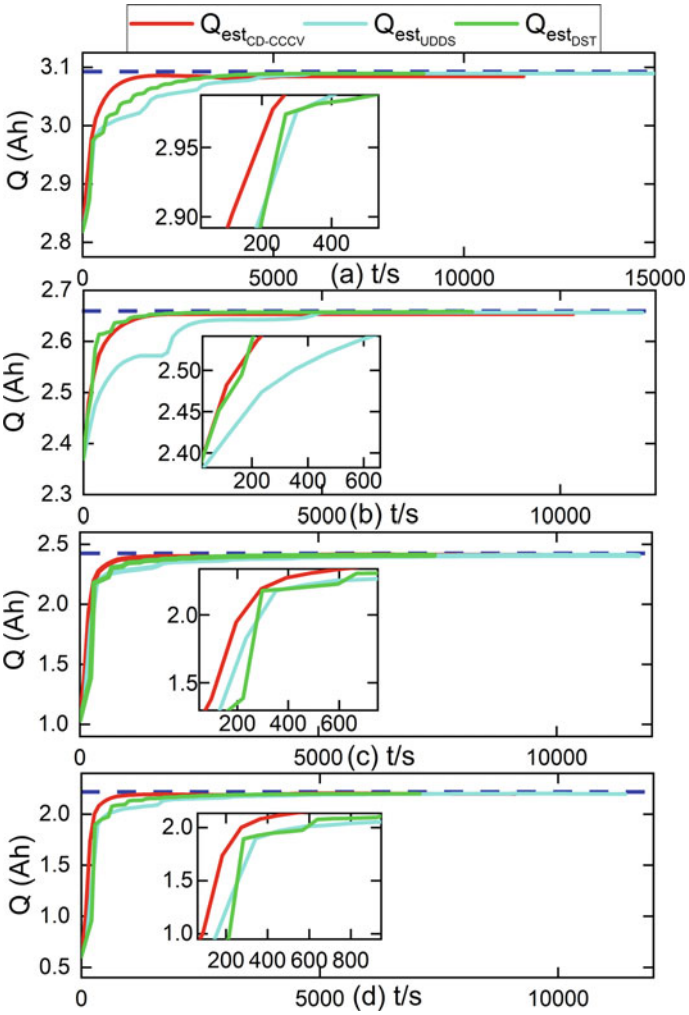

Fig. 4.32 Battery SoH estimation results with CD-CCCV, UDDS, DST tests at different ageing levels, **a** 100% SoH, **b** 86% SoH, **c** 78% SoH, and **d** 71% SoH, reprinted from [61], with permission from IEEE

mance of the derived estimator across 400 cycles under CC-CCCV scenario. Here, the capacity is predicted at each CC-CCCV cycle. Figure 4.33a plots the values of estimated capacities with blue plus symbols. The red dot symbols represent capacity measurements and the red dotted line is the interpolated curve using the measured data. It can be noted that the capacity estimates over 400 cycles could follow the red curve closely. Figure 4.33b summarizes the related capacity estimation error. Here, the mean error is 0.0241 Ah, which is within 1% of the cell nominal capacity.

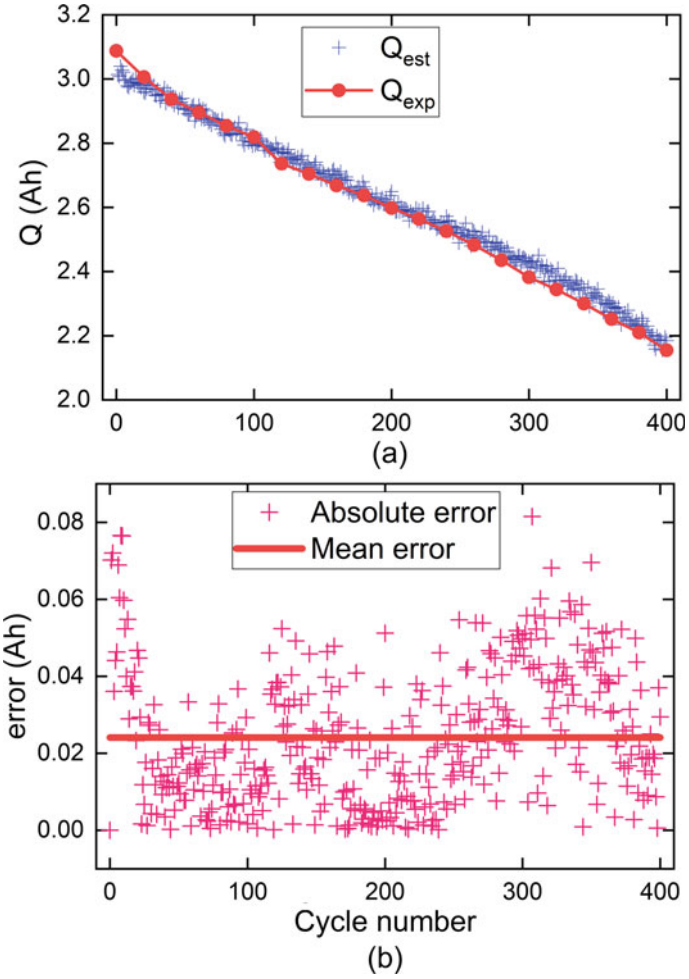

Fig. 4.33 Battery capacity estimation results: **a** results against reference values, **b** estimation error, reprinted from [61], with permission from IEEE

The statistical results reveal that the SoH estimations with the presented algorithm achieve agreeable precision over the cell lifespan.

Apart from battery SoH estimation, another key task is to estimate the variations of model parameters that relate to the dominant ageing mechanisms within a battery (loss of recyclable ions, loss of active materials, and resistance increase), thereby ensuring an accurate SoC estimate overtime. To examine the robustness of the proposed co-estimation scheme against battery ageing, the cells at four various ageing levels with the capacity of 3.088, 2.658, 2.406, and 2.199 Ah are examined. Both UDDS and DST cycles in the characterization tests are carried out to simulate the operating load profiles of dynamic EV applications. The cyclic data with CC

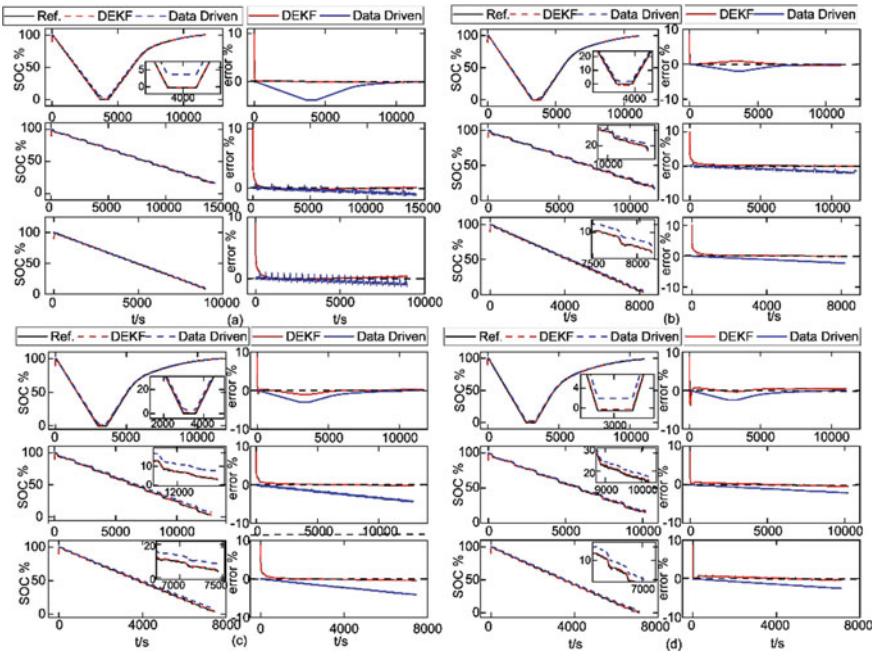

Fig. 4.34 Battery SoC estimation results with CD-CCCV (upper), UDDS (middle) and DST (bottom) cycles, **a** 100% SoH, **b** 86% SoH, **c** 78% SoH, and **d** 71% SoH, reprinted from [61], with permission from IEEE

discharging and CCCV charging is utilized. The proposed dual EKF (DEKF) SoC estimation performance is compared to the data-driven joint SoH/SoC estimation for CC-CCCV, UDDS, DST tests at four different ageing levels. The framework of the data-driven joint estimation is inspired by Refs. [65–67]. The obtained SoC estimation results under CC-CCCV, UDDS, and DST profiles with electrochemical model-based DEKF and data-driven method are shown in Fig. 4.34a–d. All the SoC estimations with DEKF are initialized with an error of 10%. For the fresh cell in Fig. 4.34a, although large initial errors of 10% are imposed, the online estimation of SoC can still quickly converge and show good agreement with the referenced SoC. According to Fig. 4.34b, when the battery parameters decay to 2.658 Ah (71% SoH), the DEKF SoC estimation performance outperforms the data-driven method. For DEKF SoC estimation, the estimation error with CC-CCCV test drops below 1% after 98 s and then converges towards less than 0.44% in a steady state. It can be noted that the SoC estimation results with UDDS and DST tests demonstrate fast convergence and high precision as well. However, the SoC estimation errors of data-driven SoC estimation are unable to converge to the true values with battery degradation. The maximum absolute errors reach 1.95%, 1.73%, and 2.28% with CC-CCCV, UDDS and DST tests, respectively. For cells with 2.406 and 2.199 Ah, similar trends can be observed as well. The data-driven SoC estimation steadily drifts away from its

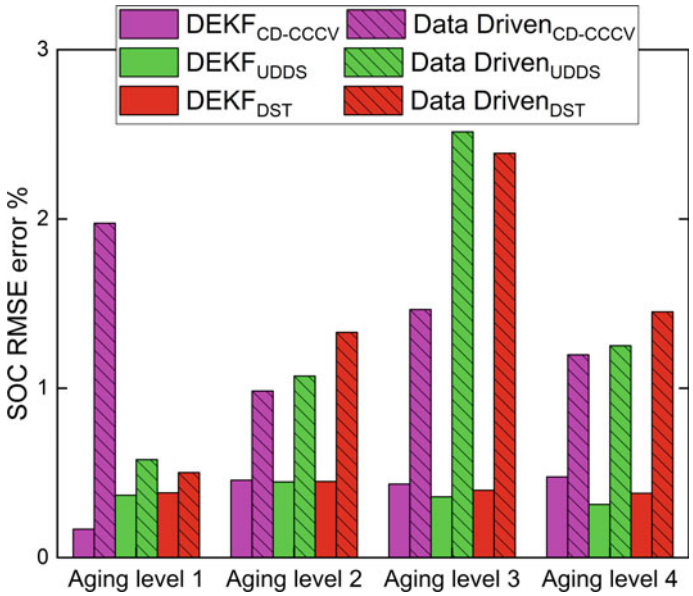

Fig. 4.35 RMSE errors of battery SoC estimation, reprinted from [61], with permission from IEEE

initial values. This leads to large errors beyond the accurate starting value of 100%. In contrast, the DEKF SoC estimation quickly converges to the reference and steadily finds its way back to a close neighbourhood of the reference value.

Figure 4.35 illustrates the RMSEs of SoC estimation at these ageing levels. Even for cells at the most degraded level 4, the corresponding RMSEs of SoC estimation with the proposed method are all within 0.48%. However, the data-driven SoC estimation results increase over 1.20%, indicating that the robustness of the data-driven SoC estimator should be strengthened by considering measurement noise and error compensation for aged cells.

Figure 4.36 shows the RMSEs of DEKF SoC estimation across 400 cycles under CC-CCCV scenario. The estimated $\theta_{0\%,n}$, $\theta_{100\%,n}$, $\varepsilon_{s,n}$ and R_f from the SoH observer are used to update the SoC estimator after each CC-CCCV cycle. The SoC estimate RMSE over a given CD-CCCV cycle almost remains constant near the averaged RMSEs throughout the life of the cell. The maximum SoC RMSE is less than 0.7%. This implies that the model is updated correctly with the estimates of $\theta_{0\%,n}$, $\theta_{100\%,n}$, $\varepsilon_{s,n}$ and R_f. It is clear that the co-estimation of SoC/SoH could not only provide electrochemical-mechanism enhanced SoH prediction at relatively slow timescale but also improve its real-time resilience to disturbance caused by battery degradation. Therefore, the SoC estimation performance is well sustained over the cell's lifespan.

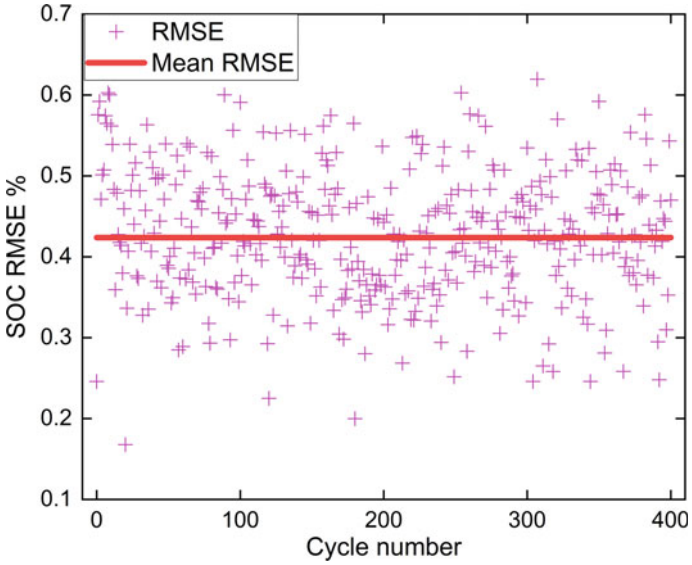

Fig. 4.36 RMSEs for battery SOC estimation versus 400 cycles, reprinted from [61], with permission from IEEE

4.3 Summary

This chapter mainly focuses on the data science-based battery operation modelling and state estimation, two basic parts for battery operation management. Specifically, three typical types of battery operation models including battery electrical model, battery thermal model, and battery coupled model are first described. Then, the fundamentals of battery SoC, SoP, SoH, and joint states estimations are introduced. The advantages and limitations of each mainstream type of state estimation method are compared and discussed. For SoC estimation, a data science-based case study using RLS and EKF is introduced. Then based upon the estimated SoC information, another data science-based case study of using the multi-constrained dynamic method to estimate battery SoP is also given. For SoH estimation, after using NSGA-II to select the optimal multiple voltage ranges, a data science-based case study is introduced to estimate SoH based on the optimized partial charging voltage profiles. After that, a data science-based case study through developing an enhanced electrochemical model to achieve high-fidelity co-estimation of SoC and SoH is presented. All these case studies could give reasonable and effective estimation results, while co-estimation is able to present better performance. These results indicate that battery states are coupled and interact with each other during operations. Satisfactory battery operation modelling and state estimations can be achieved with suitable data science solutions.

References

1. Liu K, Li K, Peng Q, Zhang C (2019) A brief review on key technologies in the battery management system of electric vehicles. Front Mech Eng 14(1):47–64
2. Rahman MA, Anwar S, Izadian A (2016) Electrochemical model parameter identification of a lithium-ion battery using particle swarm optimization method. J Power Sources 307:86–97
3. Sung W, Shin CB (2015) Electrochemical model of a lithium-ion battery implemented into an automotive battery management system. Comput Chem Eng 76:87–97
4. Han X, Ouyang M, Lu L, Li J (2015) Simplification of physics-based electrochemical model for lithium ion battery on electric vehicle. Part II: Pseudo-two-dimensional model simplification and state of charge estimation. J Power Sources 278:814–825
5. Zou C, Manzie C, Nešić D (2015) A framework for simplification of PDE-based lithium-ion battery models. IEEE Trans Control Syst Technol 24(5):1594–1609
6. Zhang L, Wang Z, Hu X, Sun F, Dorrell DG (2015) A comparative study of equivalent circuit models of ultracapacitors for electric vehicles. J Power Sources 274:899–906
7. Nejad S, Gladwin D, Stone D (2016) A systematic review of lumped-parameter equivalent circuit models for real-time estimation of lithium-ion battery states. J Power Sources 316:183–196
8. Gong X, Xiong R, Mi CC (2015) A data-driven bias-correction-method-based lithium-ion battery modeling approach for electric vehicle applications. IEEE Trans Ind Appl 52(2):1759–1765
9. Wang Q-K, He Y-J, Shen J-N, Ma Z-F, Zhong G-B (2017) A unified modeling framework for lithium-ion batteries: an artificial neural network based thermal coupled equivalent circuit model approach. Energy 138:118–132
10. Deng Z, Yang L, Cai Y, Deng H, Sun L (2016) Online available capacity prediction and state of charge estimation based on advanced data-driven algorithms for lithium iron phosphate battery. Energy 112:469–480
11. Sbarufatti C, Corbetta M, Giglio M, Cadini F (2017) Adaptive prognosis of lithium-ion batteries based on the combination of particle filters and radial basis function neural networks. J Power Sources 344:128–140
12. Li Y, Chattopadhyay P, Xiong S, Ray A, Rahn CD (2016) Dynamic data-driven and model-based recursive analysis for estimation of battery state-of-charge. Appl Energy 184:266–275
13. Xie Y, Zheng J, Hu X, Lin X, Liu K, Sun J, Zhang Y, Dan D, Xi D, Feng F (2020) An improved resistance-based thermal model for prismatic lithium-ion battery charging. Appl Therm Eng 180:115794
14. Li W, Xie Y, Liu K, Yang R, Chen B, Zhang Y (in press) An enhanced thermal model with virtual resistance technique for pouch batteries at low temperature and high current rates. IEEE J Emerg Sel Topics Power Electron. https://doi.org/10.1109/JESTPE.2021.3127892
15. Shang Y, Liu K, Cui N, Zhang Q, Zhang C (2019) A sine-wave heating circuit for automotive battery self-heating at subzero temperatures. IEEE Trans Ind Inform 16(5):3355–3365
16. Raijmakers LH, Danilov DL, Van Lammeren JP, Lammers TJ, Bergveld HJ, Notten PH (2016) Non-zero intercept frequency: an accurate method to determine the integral temperature of Li-ion batteries. IEEE Trans Ind Electron 63(5):3168–3178
17. Lee K-T, Dai M-J, Chuang C-C (2017) Temperature-compensated model for lithium-ion polymer batteries with extended Kalman filter state-of-charge estimation for an implantable charger. IEEE Trans Ind Electron 65(1):589–596
18. Zhu C, Han J, Zhang H, Lu F, Liu K, Zhang X (in press) Modeling and control of an integrated self-heater for automotive batteries based on traction motor drive reconfiguration. IEEE J Emerg Sel Topics Power Electron. https://doi.org/10.1109/JESTPE.2021.3119599
19. Shang Y, Liu K, Cui N, Wang N, Li K, Zhang C (2019) A compact resonant switched-capacitor heater for lithium-ion battery self-heating at low temperatures. IEEE Trans Power Electron 35(7):7134–7144
20. Guo M, Kim G-H, White RE (2013) A three-dimensional multi-physics model for a Li-ion battery. J Power Sources 240:80–94

21. Jeon DH, Baek SM (2011) Thermal modeling of cylindrical lithium ion battery during discharge cycle. Energy Convers Manag 52(8–9):2973–2981
22. Jaguemont J, Omar N, Martel F, Van Den Bossche P, Van Mierlo J (2017) Streamline three-dimensional thermal model of a lithium titanate pouch cell battery in extreme temperature conditions with module simulation. J Power Sources 367:24–33
23. Shah K, Vishwakarma V, Jain A (2016) Measurement of multiscale thermal transport phenomena in Li-ion cells: a review. J Electrochem Energy Convers Storage 13(3)
24. Chen D, Jiang J, Li X, Wang Z, Zhang W (2016) Modeling of a pouch lithium ion battery using a distributed parameter equivalent circuit for internal non-uniformity analysis. Energies 9(11):865
25. Hu X, Asgari S, Yavuz I, Stanton S, Hsu CC, Shi ZY, Wang B, Chu HK, A transient reduced order model for battery thermal management based on singular value decomposition. In: Proceedings of IEEE energy conversion congress and exposition (ECCE), Pittsburgh, PA, 2014, pp 3971–3976
26. Lin X, Perez HE, Mohan S, Siegel JB, Stefanopoulou AG, Ding Y, Castanier MP (2014) A lumped-parameter electro-thermal model for cylindrical batteries. J Power Sources 257:1–11
27. Perez HE, Hu X, Dey S, Moura SJ (2017) Optimal charging of Li-ion batteries with coupled electro-thermal-aging dynamics. IEEE Trans Veh Technol 66(9):7761–7770
28. Dey S, Ayalew B (2017) Real-time estimation of lithium-ion concentration in both electrodes of a lithium-ion battery cell utilizing electrochemical–thermal coupling. J Dyn Syst Meas Control 139(3)
29. Goutam S, Nikolian A, Jaguemont J, Smekens J, Omar N, Bossche PVD, Van Mierlo J (2017) Three-dimensional electro-thermal model of Li-ion pouch cell: analysis and comparison of cell design factors and model assumptions. Appl Therm Eng 126:796–808
30. Jiang J, Ruan H, Sun B, Zhang W, Gao W, Zhang L (2016) A reduced low-temperature electro-thermal coupled model for lithium-ion batteries. Appl Energy 177:804–816
31. Basu S, Hariharan KS, Kolake SM, Song T, Sohn DK, Yeo T (2016) Coupled electrochemical thermal modelling of a novel Li-ion battery pack thermal management system. Appl Energy 181:1–13
32. Hu X, Feng F, Liu K, Zhang L, Xie J, Liu B (2019) State estimation for advanced battery management: key challenges and future trends. Renew Sustain Energy Rev 114:109334
33. Hannan MA, Lipu MH, Hussain A, Mohamed A (2017) A review of lithium-ion battery state of charge estimation and management system in electric vehicle applications: challenges and recommendations. Renew Sustain Energy Rev 78:834–854
34. Liu K, Tang X, Widanage WD (2020) Light-weighted battery state of charge estimation based on the sigma-delta technique. IFAC-PapersOnLine 53(2):12446–12451
35. Chang W-Y (2013) The state of charge estimating methods for battery: a review. Int Sch Res Notices
36. Zheng F, Xing Y, Jiang J, Sun B, Kim J, Pecht M (2016) Influence of different open circuit voltage tests on state of charge online estimation for lithium-ion batteries. Appl Energy 183:513–525
37. Zou C, Hu X, Dey S, Zhang L, Tang X (2017) Nonlinear fractional-order estimator with guaranteed robustness and stability for lithium-ion batteries. IEEE Trans Ind Electron 65(7):5951–5961
38. Guo Y, Yang Z, Liu K, Zhang Y, Feng W (2021) A compact and optimized neural network approach for battery state-of-charge estimation of energy storage system. Energy 219:119529
39. Meng J, Luo G, Gao F (2015) Lithium polymer battery state-of-charge estimation based on adaptive unscented Kalman filter and support vector machine. IEEE Trans Power Electron 31(3):2226–2238
40. Farmann A, Sauer DU (2016) A comprehensive review of on-board State-of-Available-Power prediction techniques for lithium-ion batteries in electric vehicles. J Power Sources 329:123–137
41. Wang Y, Pan R, Liu C, Chen Z, Ling Q (2018) Power capability evaluation for lithium iron phosphate batteries based on multi-parameter constraints estimation. J Power Sources 374:12–23

42. Feng T, Yang L, Zhao X, Zhang H, Qiang J (2015) Online identification of lithium-ion battery parameters based on an improved equivalent-circuit model and its implementation on battery state-of-power prediction. J Power Sources 281:192–203
43. Tang X, Liu K, Liu Q, Peng Q, Gao F (2021) Comprehensive study and improvement of experimental methods for obtaining referenced battery state-of-power. J Power Sources 512:230462
44. Pei L, Zhu C, Wang T, Lu R, Chan C (2014) Online peak power prediction based on a parameter and state estimator for lithium-ion batteries in electric vehicles. Energy 66:766–778
45. Tang X, Gao F, Liu K, Liu Q, Foley AM (in press) A balancing current ratio based state-of-health estimation solution for lithium-ion battery pack. IEEE Trans Ind Electron. https://doi.org/10.1109/TIE.2021.3108715
46. Hu X, Yuan H, Zou C, Li Z, Zhang L (2018) Co-estimation of state of charge and state of health for lithium-ion batteries based on fractional-order calculus. IEEE Trans Veh Technol 67(11):10319–10329
47. Tang X, Liu K, Lu J, Liu B, Wang X, Gao F (2020) Battery incremental capacity curve extraction by a two-dimensional Luenberger–Gaussian-moving-average filter. Appl Energy 280:115895
48. Lu J, Wu TP, Amine K (2017) State-of-the-art characterization techniques for advanced lithium-ion batteries. Nat Energy 2(3)
49. Waag W, Sauer DU (2013) Adaptive estimation of the electromotive force of the lithium-ion battery after current interruption for an accurate state-of-charge and capacity determination. Appl Energy 111:416–427
50. Stroe D-I, Schaltz E (2019) Lithium-ion battery state-of-health estimation using the incremental capacity analysis technique. IEEE Trans Ind Appl 56(1):678–685
51. Xiong R, Li L, Tian J (2018) Towards a smarter battery management system: a critical review on battery state of health monitoring methods. J Power Sources 405:18–29
52. Li Y, Liu K, Foley AM, Zülke A, Berecibar M, Nanini-Maury E, Van Mierlo J, Hoster HE (2019) Data-driven health estimation and lifetime prediction of lithium-ion batteries: a review. Renew Sustain Energy Rev 113:109254
53. Meng J, Cai L, Stroe D-I, Luo G, Sui X, Teodorescu R (2019) Lithium-ion battery state-of-health estimation in electric vehicle using optimized partial charging voltage profiles. Energy 185:1054–1062
54. Feng F, Hu X, Liu K, Che Y, Lin X, Jin G, Liu B (2020) A practical and comprehensive evaluation method for series-connected battery pack models. IEEE Trans Transp Electrification 6(2):391–416
55. Liu K, Li K, Peng Q, Guo Y, Zhang L (2018) Data-driven hybrid internal temperature estimation approach for battery thermal management. Complexity 2018
56. Hu C, Youn BD, Chung J (2012) A multiscale framework with extended Kalman filter for lithium-ion battery SOC and capacity estimation. Appl Energy 92:694–704
57. Zou C, Manzie C, Nešić D, Kallapur AG (2016) Multi-time-scale observer design for state-of-charge and state-of-health of a lithium-ion battery. J Power Sources 335:121–130
58. Dong G, Wei J, Chen Z (2016) Kalman filter for onboard state of charge estimation and peak power capability analysis of lithium-ion batteries. J Power Sources 328:615–626
59. Feng F, Teng S, Liu K, Xie J, Xie Y, Liu B, Li K (2020) Co-estimation of lithium-ion battery state of charge and state of temperature based on a hybrid electrochemical-thermal-neural-network model. J Power Sources 455:227935
60. Wei Z, Zhao J, Ji D, Tseng KJ (2017) A multi-timescale estimator for battery state of charge and capacity dual estimation based on an online identified model. Appl Energy 204:1264–1274
61. Gao Y, Liu K, Zhu C, Zhang X, Zhang D (2022) Co-estimation of state-of-charge and state-of-health for lithium-ion batteries using an enhanced electrochemical model. IEEE Trans Ind Electron 69(3):2684–2696
62. Moura SJ, Chaturvedi NA, Krstić M (2014) Adaptive partial differential equation observer for battery state-of-charge/state-of-health estimation via an electrochemical model. J Dyn Syst Meas Control 136(1)

63. Zhang X, Gao Y, Guo B, Zhu C, Zhou X, Wang L, Cao J (2020) A novel quantitative electrochemical aging model considering side reactions for lithium-ion batteries. Electrochim Acta 343:136070
64. Tanim TR, Rahn CD, Wang C-Y (2015) State of charge estimation of a lithium ion cell based on a temperature dependent and electrolyte enhanced single particle model. Energy 80:731–739
65. Klass V, Behm M, Lindbergh G (2015) Capturing lithium-ion battery dynamics with support vector machine-based battery model. J Power Sources 298:92–101
66. Feng X, Weng C, He X, Han X, Lu L, Ren D, Ouyang M (2019) Online state-of-health estimation for Li-ion battery using partial charging segment based on support vector machine. IEEE Trans Veh Technol 68(9):8583–8592
67. Song Y, Liu D, Liao H, Peng Y (2020) A hybrid statistical data-driven method for on-line joint state estimation of lithium-ion batteries. Appl Energy 261:114408